A&A 674, A81 (2023)
https://doi.org/10.1051/0004-6361/202345945

Astronomy & Astrophysics

Polarimetry of hydrogen-poor superluminous supernovae

M. Pursiainen[1], G. Leloudas[1], A. Cikota[2], M. Bulla[3,4,5], C. Inserra[6], F. Patat[7], J. C. Wheeler[8], A. Aamer[9], A. Gal-Yam[10], J. Maund[11], M. Nicholl[9], S. Schulze[12], J. Sollerman[12], and Y. Yang[13]

[1] DTU Space, National Space Institute, Technical University of Denmark, Elektrovej 327, 2800 Kgs. Lyngby, Denmark
e-mail: miipu@space.dtu.dk
[2] Gemini Observatory/NSF's NOIRLab, Casilla 603, La Serena, Chile
[3] Department of Physics and Earth Science, University of Ferrara, Via Saragat 1, 44122 Ferrara, Italy
[4] INFN, Sezione di Ferrara, Via Saragat 1, 44122 Ferrara, Italy
[5] INAF, Osservatorio Astronomico d'Abruzzo, Via Mentore Maggini snc, 64100 Teramo, Italy
[6] Cardiff Hub for Astrophysics Research and Technology, School of Physics & Astronomy, Cardiff University, Queens Buildings, The Parade, Cardiff CF24 3AA, UK
[7] European Southern Observatory, Karl-Schwarzschild-Str. 2, 85748 Garching b. München, Germany
[8] Department of Astronomy, University of Texas at Austin, 2515 Speedway, Austin, TX 78712, USA
[9] Birmingham Institute for Gravitational Wave Astronomy and School of Physics and Astronomy, University of Birmingham, Edgbaston Park Rd, Birmingham B15 2TT, UK
[10] Department of Particle Physics and Astrophysics, Weizmann Institute of Science, 234 Herzl Street, 76100 Rehovot, Israel
[11] Department of Physics and Astronomy, University of Sheffield, Hicks Building, Hounsfield Road, Sheffield S3 7RH, UK
[12] The Oskar Klein Centre, Department of Astronomy, Stockholm University, AlbaNova 10691, Stockholm, Sweden
[13] Department of Astronomy, University of California, 501 Campbell Hall #3411, Berkeley, CA 94720-3411, USA

Received 19 January 2023 / Accepted 18 March 2023

ABSTRACT

We present linear polarimetry for seven hydrogen-poor superluminous supernovae (SLSNe-I) of which only one has previously published polarimetric data. The best-studied event is SN 2017gci, for which we present two epochs of spectropolarimetry at +3 d and +29 d post-peak in rest frame, accompanied by four epochs of imaging polarimetry up to +108 d. The spectropolarimetry at +3 d shows increasing polarisation degree P towards the redder wavelengths and exhibits signs of axial symmetry, but at +29 d, $P \sim 0$ throughout the spectrum, implying that the photosphere of SN 2017gci evolved from a slightly aspherical configuration to a more spherical one in the first month post-peak. However, an increase of P to ∼0.5% at ∼+55 d accompanied by a different orientation of the axial symmetry compared to +3 d implies the presence of additional sources of polarisation at this phase. The increase in polarisation is possibly caused by interaction with circumstellar matter (CSM), as already suggested by a knee in the light curve and a possible detection of broad Hα emission at the same phase. We also analysed the sample of all 16 SLSNe-I with polarimetric measurements to date. The data taken during the early spectroscopic phase show consistently low polarisation, indicating at least nearly spherical photospheres. No clear relation between the polarimetry and spectral phase was seen when the spectra resemble Type Ic SNe during the photospheric and nebular phases. The light-curve decline rate, which spans a factor of eight, also shows no clear relation with the polarisation properties. While only slow-evolving SLSNe-I have shown non-zero polarisation, the fast-evolving ones have not been observed at sufficiently late times to conclude that none of them exhibit changing P. However, the four SLSNe-I with increasing polarisation degree also have irregular light-curve declines. For up to half of them, the photometric, spectroscopic, and polarimetric properties are affected by CSM interaction. As such, CSM interaction clearly plays an important role in understanding the polarimetric evolution of SLSNe-I.

Key words. supernovae: general – polarization – techniques: polarimetric

1. Introduction

Superluminous supernovae (SLSNe) are an enigmatic class of stellar explosions that are characterised by exceptionally bright, often long-lived light curves (e.g. Gal-Yam et al. 2009; Pastorello et al. 2010; Chomiuk et al. 2011; Quimby et al. 2011). While it has been nearly two decades since the first discovered events (e.g. SN 2005ap; Quimby et al. 2007), the mechanism powering their extreme luminosities is still a topic of debate (for reviews, see e.g. Gal-Yam 2012, 2019; Moriya et al. 2018; Nicholl 2021). It is difficult to explain the photometric evolution of most SLSNe with the decay of radioactive ^{56}Ni – the canonical power source of Type Ia and Ibc supernovae (SNe) – and alternative scenarios have been sought. The most popular models are either related to a spin-down of a highly magnetised neutron star (magnetar) formed in the aftermath of the core collapse (e.g. Woosley 2010; Kasen & Bildsten 2010) or to some manner of interaction between the SN ejecta and circumstellar material (CSM; e.g. Chevalier & Irwin 2011), but the importance of jets has also been discussed (e.g. Soker & Gilkis 2017; Soker 2022). However, despite the abundant data sets of both photometry (e.g. De Cia et al. 2018; Angus et al. 2019; Chen et al. 2023a) and spectroscopy (e.g. Quimby et al. 2018), there is no clear consensus on the most viable scenario.

One way to gain further insight into the nature of the energy source of SLSNe is to investigate the evolution of the photospheric shape of the unresolved SNe via polarimetry. The continuum polarisation is induced by Thomson scattering

of light from free electrons that are abundant in the SN ejecta (Shapiro & Sutherland 1982) and thus polarimetry directly probes the geometry of the photosphere. In the case where the SN has a circular projection on the sky, there is no prevalent direction for the polarised light and zero polarisation is expected. However, if the projection deviates from a perfect circle due to intrinsic asphericity of the photosphere, a non-zero polarisation signal is produced. For a more detailed description of polarimetry in the context of SNe, see Wang & Wheeler (2008) and Patat (2017). For SLSNe, polarimetry is potentially a vital tool. In the case where they are powered by an internal engine such as a magnetar, the energy input is expected to be aspherical. As the ejecta expand over time, the electron density drops, and a more aspherical configuration of the inner layers of the ejecta should be revealed to the observer. The field of studying the geometry of SLSNe is still in its infancy. Only ten hydrogen-deficient SLSNe-I have any polarimetric data in the literature, of which only three have spectropolarimetry that provided concrete results.

Perhaps the best-studied case of SLSNe-I with polarimetry is SN 2015bn. The slowly evolving event was observed in both spectropolarimetry (Inserra et al. 2016) and broad-band imaging polarimetry (Leloudas et al. 2017). Two epochs of spectropolarimetry were obtained at −24 days before and +27 days after peak and this follows a well-defined axial symmetry. The broad-band polarimetry spanned nine epochs between −20 and +46 d with an increase of polarisation from ∼0.5% to >1%. For a hypothetical oblate spheroid photosphere, which follows an inverse-square power law radial density distribution, the broad-band polarisation indicates an axial ratio of >1.2 (Höflich 1991). Both spectropolarimetry and broad-band polarimetry suggest an increased deviation from spherical symmetry toward the deeper layers of the ejecta. Leloudas et al. (2017) proposed that the ejecta underwent a structural change at around +20 d, when the photospheric emission shifted from an outer layer dominated by C and O to a more aspherical inner core dominated by heavier, freshly synthesised material. This is supported by the simultaneous spectral change noted by Nicholl et al. (2016b).

The slowly declining SN 2017egm was observed near maximum light in spectropolarimetry (Bose et al. 2018) and broad-band polarimetry (Maund et al. 2019). The spectropolarimetry, as reanalysed by Saito et al. (2020), shows a polarisation of ∼0.2% near peak that was not strongly dependent on wavelength. These authors suggested a modest departure from spherical symmetry with an axial ratio of ∼1.05. Maund et al. (2019) did not detect intrinsic polarisation at four epochs spanning from +4 d to +19 d. Saito et al. (2020) report Subaru spectropolarimetry of SN 2017egm at +185 d, the only such measurement of a SLSN at this late stage. These latter authors find that the polarisation increased to ∼0.8%, corresponding to an axial ratio of ∼1.2. The late polarisation shows a nearly constant position angle over the wavelength range, suggesting an axisymmetric structure similar to that of SN 2015bn, and Saito et al. (2020) conclude that the inner ejecta are more aspherical than the outer ejecta.

Recently, Pursiainen et al. (2022) analysed two epochs of spectropolarimetry of SN 2018bsz – the most nearby SLSN-I to date at $z = 0.0267$ (see e.g. Anderson et al. 2018; Chen et al. 2021) – along an extensive spectroscopic data set. These authors conclude that the polarimetric and spectroscopic properties of SN 2018bsz show clear evidence of the SN ejecta interacting with close-by, highly aspherical CSM. After the explosion, the expanding ejecta quickly overtook the CSM and the first epoch of polarimetry at +10 d was probing the geometry of the ejecta. However, as the photosphere receded, the aspherical CSM re-emerged as indicated by a multi-component Hα line that appeared at ∼+30 d. Therefore, the second epoch of polarimetry at +40 d probed the photosphere that was strongly influenced by CSM, resulting in a drastic change of the polarisation properties. While the authors could not determine the interstellar polarisation (ISP) induced by dichroic absorption of non-spherical dust grains partially aligned by the interstellar magnetic field, assuming that the ejecta at +10 d is spherically symmetric, a 1.8% rise of polarisation at +40 d can be identified. Furthermore, Maund et al. (2021) analysed complementary imaging polarimetry and obtained one detection of $P \sim 2.0 \pm 0.5\%$ at +19 d.

There are also a number of SLSNe-I that have been observed exclusively with broad-band polarimetry. Leloudas et al. (2015a) presented imaging polarimetry of the fast-evolving SLSN-I LSQ14mo spanning from −7 to +18 days. The level of polarisation was constant at ∼0.5% and most likely attributable to the ISP. While this might be an indication of a small deviation from spherical symmetry, Inserra et al. (2016) noted that LSQ14mo was fainter than SN 2015bn, and it is possible that the data were of an insufficient signal-to-noise ratio (S/N), and an asymmetric geometry like that of SN 2015bn cannot be completely ruled out. Low levels of broad-band polarisation have also been obtained for other SLSNe-I near peak brightness. Cikota et al. (2018) presented broad-band polarimetry of the fast-evolving PS17bek at four epochs between −4 and +21 days and no polarisation signal intrinsic to the SN was detected. Lee (2020) reported an insignificant detection of polarisation in a single epoch of near-peak imaging polarimetry for SN 2020ank. Lee (2019) also shows that the 1.9% polarisation of SN 2018hti measured around its peak luminosity is consistent with the level of the ISP. On the other hand, Poidevin et al. (2022) presented imaging polarimetry of SN 2020znr at ∼+30 d and ∼+290 d. Based on the non-detections at both epochs, these latter authors suggest that the high ejecta mass of the exceptionally slowly evolving SLSN-I may have prevented the inner geometry of the SN from being correctly probed. Finally, Poidevin et al. (2023) provide imaging polarimetry for two SLSNe-I. The single epoch of SN 2021bnw at +81 d showed no departure from symmetry, but the four epochs of SN 2021fpl between +2 d and +43 d showed consistent polarisation around 1%. Based on spectral comparison, the authors concluded that SN 2021fpl underwent a spectral transition similarly to SN 2015bn but at an earlier phase, possibly explaining the consistently high polarisation.

Additionally, Cikota et al. (2018) presented the first circular polarimetry for two SLSNe-I. The fast-evolving PS17bek was observed around peak and the slow-evolving OGLE16dmu at +100 d. Neither event showed evidence of circular polarisation. The non-detection did not constrain the magnetar scenario, because a signal would only be expected close to the surface of the magnetar.

The scarce sample of polarimetric data for SLSNe-I shows that we are far from having a complete view of the time-evolving 3D structure of these spectacular events. While some events show distinct evidence for axisymmetry, others do not. It is not clear whether SLSNe-I with fast-evolving light curves have a different geometry from the slow-evolving ones, nor whether the spectral phases of the polarimetry show any polarimetric tendency. Furthermore, the evidence that some SLSNe-I show greater asymmetry in deeper ejecta, as do standard core-collapse supernovae, has not yet been converted into quantitative evidence for an internal engine, such as a magnetar. Instead, CSM has been identified in a number of SLSNe-I

Table 1. 16 SLSNe-I with linear polarimetry.

SN	Peak MJD	z	Refs.
LSQ14mo	56697.1	0.2560	[2]
SN 2015bn	57102.5	0.1136	[3,4]
PS17bek	57814.6	0.3099	[5]
SN 2017egm	57926.2	0.0310	[**1**,6,7,8]
SN 2017gci	57986.8	0.0870	[**1**]
SN 2018bgv	58256.3	0.0790	[**1**]
SN 2018bsz	58267.5	0.0267	[9,10]
SN 2018ffj [(a)]	58337.6	0.2340	[**1**]
SN 2018hti	58462.1	0.0614	[11]
SN 2018ibb	58455.0	0.1660	[**1**,12]
SN 2019neq	58734.0	0.1075	[**1**]
SN 2020ank	58898.5	0.2485	[13]
SN 2020tcw	59130.1	0.0645	[**1**]
SN 2020znr	59227.5	0.1000	[14]
SN 2021bnw	59264.5	0.0980	[15]
SN 2021fpl	59342.5	0.1150	[15]

Notes. Peak MJD refers to the observed r/V band peak. [(a)] Caught on decline, MJD of first detection shown.
References. [1] This study (in bold); [2] Leloudas et al. (2015a); [3] Inserra et al. (2016); [4] Leloudas et al. (2017); [5] Cikota et al. (2018); [6] Bose et al. (2018); [7] Maund et al. (2019); [8] Saito et al. (2020); [9] Maund et al. (2021); [10] Pursiainen et al. (2022); [11] Lee (2019); [12] Schulze et al. (2023); [13] Lee (2020); [14] Poidevin et al. (2022); [15] Poidevin et al. (2023).

(e.g. Yan et al. 2015, 2017; Lunnan et al. 2018; Pursiainen et al. 2022) and the irregular light curves seen in many SLSNe-I (see e.g. Hosseinzadeh et al. 2021; Chen et al. 2023b) suggests that CSM interaction may play a role even in SLSNe-I that display no obvious spectral signatures attributed to CSM.

Here we present polarimetric data for seven SLSNe-I of which only SN 2017egm has previously published polarimetric observations. In particular, we present two epochs of spectropolarimetry for SN 2017gci with complementary imaging polarimetry. We also perform a polarimetric sample analysis of SLSNe-I. In Sect. 2 we present the observations and the data-reduction procedures and in Sect. 3 we discuss the ISP estimation. In Sect. 4 we focus on the analysis of spectral and imaging polarimetry of SN 2017gci and in Sect. 5 we investigate the sample properties of all SLSNe-I with polarimetry. We conclude our study in Sect. 6.

2. Observations and data reduction

Table 1 provides an overview of the SLSNe-I with linear polarimetric observations to date. Only ten events are available in the literature and the sample we present in this paper increases the number of SLSNe-I with polarimetry by ~60%. For SN 2017gci, we provide both spectral and imaging polarimetry taken with the European Southern Observatory (ESO) Very Large Telescope (VLT; Sect. 2.1). For SN 2018ibb, we present four epochs of VLT imaging polarimetry. The details of the reduction and in-depth analysis of the SN is presented in Schulze et al. (2023). The five remaining SLSNe-I were observed in the imaging polarimetry mode at the Nordic Optical Telescope (NOT; Sect. 2.2). All values of P presented in this paper have been corrected for polarisation bias (e.g. Simmons & Stewart 1985; Wang et al. 1997) following Plaszczynski et al. (2014).

2.1. VLT spectral and imaging polarimetry of SN 2017gci

We observed SN 2017gci with the FOcal Reducer and low dispersion Spectrograph (FORS2; Appenzeller et al. 1998) mounted on the Cassegrain focus of the VLT at Cerro Paranal in Chile, in both spectral (PMOS) and imaging polarimetric (IPOL) modes. Spectropolarimetry was obtained at two epochs, on 25/26 Aug. 2017 and 22 Sep. 2017 corresponding to +3.3 and +29.0 rest frame days relative to the peak brightness, respectively. All observations were conducted with the 300V grism. Spectropolarimetry data were obtained using a 1″ slit. The absence of the GG435 order-sorting filter is adopted intentionally to extend the wavelength coverage in the blue. Complementary imaging polarimetry was obtained at four epochs on 2017-08-29, 2017-09-23, 2017-10-19 and 2017-12-17, corresponding to +7.0, +29.9, +53.8 and +108.0 d in rest frame with the $V_{\rm HIGH}$ FORS2 standard filter (λ_0 = 555 nm, $FWHM$ = 123.2 nm). All observations were obtained at four half-wave retarder plate (HWP) angles (0°, 22.5°, 45°, 67.5°) per cycle. The spectropolarimetry was reduced using standard procedures with `IRAF` (for details see Cikota et al. 2017). Furthermore, we used wavelet decomposition to reduce the noise of the flux spectra of individual ordinary and extraordinary beams (o and e beams hereafter; Cikota et al. 2019). The resulting spectra were compared against the original ones to ensure that no systematic errors were introduced. The imaging polarimetry was also reduced using standard routines (for details, see e.g. Leloudas et al. 2015a, 2017). The log of the VLT observations is given in Table B.1.

2.2. NOT imaging polarimetry

We analyse imaging polarimetry of five SLSNe-I taken with the Alhambra Faint Object Spectrograph and Camera (ALFOSC) mounted on the 2.56 m NOT at La Palma, Spain. Most observations were taken with V band filter, but for SN 2017egm, R and I were also used. Additionally, we observed SN 2019szu approximately one month after its peak brightness. However, as we explain below, the low S/N of the observation renders the results unreliable, and the SN is excluded from the analysis. All observations were obtained at four HWP angles (0°, 22.5°, 45°, 67.5°). The observation logs for the five SNe are presented in Tables B.2–B.6.

For the NOT imaging polarimetry, a custom pipeline was developed that uses `source extractor` (Bertin & Arnouts 1996) for the photometry. The aperture sizes were determined based on the `source extractor`-estimated FWHM. All images of an individual epoch (four images per cycle) were investigated, and the smallest FWHM of the o and e beams was selected as the FWHM of that epoch. In each frame, the FWHM was estimated based on the SN and the bright stars in the field.

Considering that the imaging polarimetry mode of ALFOSC tends to elongate the point-spread function of the sources in o and e beams differently (see e.g. Leloudas et al. 2017), the only feasible way to ensure that the same fraction of light was retrieved for every e beam and o beam source over the four angles is to enclose the majority of the target flux in the aperture. While a smaller aperture size increases the S/N, and as such is ideal for photometry, the fraction of light in the o and e beams might be disproportionate, which induces spurious polarisation in the observation. However, with larger aperture the amount of light from the target no longer increases but the S/N decreases. In our experience, an aperture of $2-3 \times FWHM$ is optimal and in this paper all presented NOT imaging polarimetry values are obtained with an aperture of $2 \times FWHM$. We carried

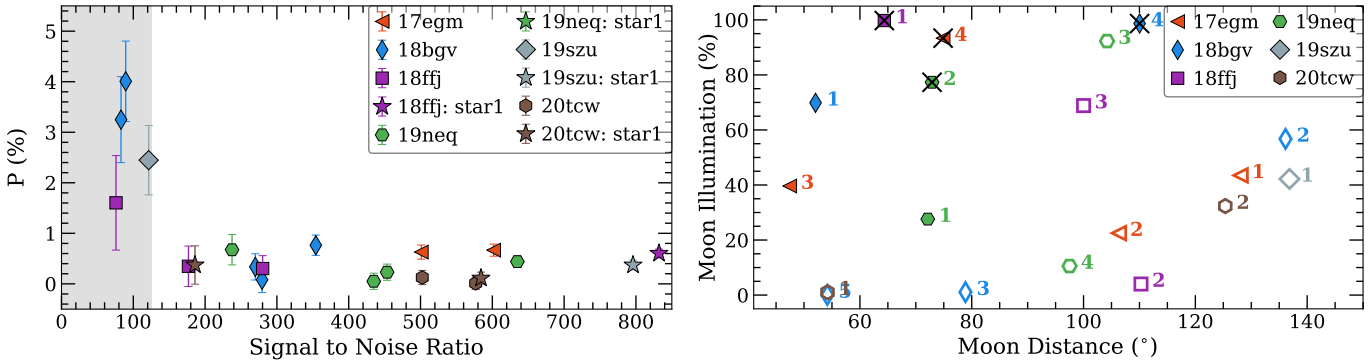

Fig. 1. Left: derived polarisation degree P (%) against the average S/N of the target for the NOT/ALFOSC imaging polarimetry in the V band. The P values have been corrected for polarisation bias following Plaszczynski et al. (2014). High values of polarisation degree are found only below $S/N \sim 125$ (grey region), implying these measurements are untrustworthy. We note that the single epoch of SN 2019szu is also shown in the figure, but is excluded from the analysis because of the low S/N. Right: moon illumination against the SN–Moon separation at the time of the observations. The respective epoch of each SN is shown next to each marker. The epochs that were identified as questionable in comparison to neighbouring observations have been crossed in black. Open markers denote epochs when the Moon was below the horizon. The questionable observations were taken during high lunar illumination, implying that it affects the results, rendering them unreliable.

out extensive checks to verify the impact of the aperture size on the results. All results were found to be consistent with respect to the output of an alternative pipeline (Leloudas et al. 2022) that utilises `DAOPHOT` (Stetson 1987).

We find that the ALFOSC imaging polarimetry yields unreliable results under certain conditions. First, we find that the measured values of polarisation tend to be systematically higher when the S/N of the target is $\lesssim$125, as shown in Fig. 1 (left), implying that these results are untrustworthy. This is likely a direct result of the low S/N. As polarimetry is based on flux differences between the o and e beams, the higher uncertainty can induce a false polarimetric signal. While the applied polarimetric bias correction should alleviate the issue, the corrections are statistical and designed assuming high S/N and are therefore not applicable. While it is possible that some of these observations truly show high polarisation, we exclude them from the analysis due to their uncertain nature.

Furthermore, the data taken during high lunar illumination (~75%) when the Moon was above the horizon appear to be unreliable. We identified several observational epochs as questionable, as the results show significant offset in comparison to neighbouring epochs for either the SN or a field star despite a high S/N. As shown in Fig. 1 (right), these observations were taken during high lunar illumination, implying that this latter affects the observed polarisation signal. This is likely caused by Rayleigh scattering of the lunar photons in the atmosphere, the effect of which is the strongest at 90°. Any scattering process inherently induces linear polarisation perpendicular to the plane of scattering. As such, the Moon always creates polarised background emission and during a bright Moon this can dominate the polarised flux compared to the polarised signal extracted from the SN. Therefore, unless the background is perfectly estimated in the analysis, the background polarisation can affect the measured values. The epochs highlighted in Fig. 1 (right) are as follows:

- The first epoch of SN 2018ffj: the SN itself had a low S/N (~80, see Table B.7 and Fig. C.5), but a comparison star in the same field of view (FOV) has $S/N \sim 800$ and should be reliable. However, the Stokes Q and U parameters are clearly offset from the latter two measurements (see Fig. C.3).
- The second epoch of SN 2019neq: the Stokes Q and U parameters are at an offset in comparison to the other epochs (Fig. C.5).

Table 2. ISPs used in this paper.

SN	Q_{ISP} (%)	U_{ISP} (%)	P_{ISP} (%)
SN 2017gci	−0.50 ± 0.01	−0.02 ± 0.01	0.50 ± 0.01
SN 2017egm [a]	0.29 ± 0.34	−0.40 ± 0.38	0.49 ± 0.38
SN 2018bgv [b]	0.00 ± 0.00	0.00 ± 0.00	0.00 ± 0.00
SN 2018ffj	0.09 ± 0.02	−0.08 ± 0.02	0.12 ± 0.02
SN 2019neq	0.27 ± 0.03	−0.18 ± 0.03	0.32 ± 0.03
SN 2020tcw	−0.16 ± 0.11	−0.03 ± 0.11	0.17 ± 0.11

Notes. [a] From Saito et al. (2020). [b] Based on Heiles (2000).

- The fourth epoch of SN 2017egm: even the prominent host galaxy is not visible in the image, rendering any analysis impossible.
- The fourth epoch of SN 2018bgv: high values of Q and U (Fig. C.5) and the low S/N is likely (or at least partially) due to the high lunar illumination.

We also note that while the Stokes Q and U parameters at the first epoch of SN 2018bgv are found to be similar to the two reliable epochs (see Fig. C.5), the observations were taken during high lunar illumination and are likely affected by it. Therefore, we exclude this epoch from the analysis as well. Finally, we note that as the low background level was measured when the bright Moon was below the horizon, we consider the corresponding epochs to be reliable.

3. ISP correction

One of the most crucial steps in analysing polarimetric data is to perform a correction for ISP introduced by dust grains between the target and the observer. Not only can this completely dominate the observed polarisation signature (see e.g. Stevance et al. 2019), but due to its vector nature it can both introduce and weaken the observed polarisation degree. Therefore, in order to investigate the intrinsic polarisation of SNe, the effect of ISP has to be carefully estimated and removed. Unfortunately, there is no unambiguous way to determine the level of this type of polarisation. A summary of the commonly used methods to estimate ISP is provided by Stevance et al. (2020). In the present paper, we estimate the ISPs by measuring them from the reliable,

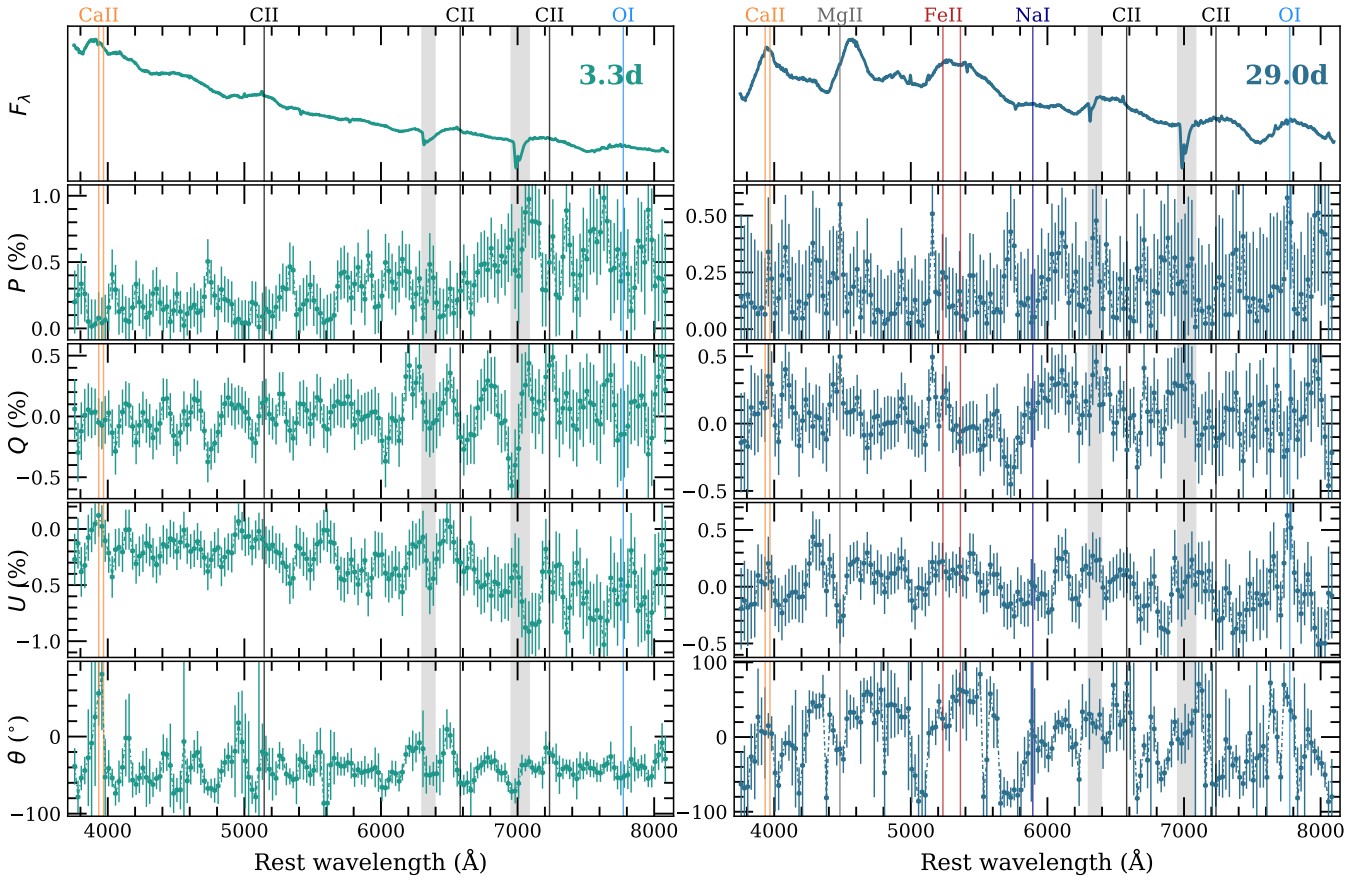

Fig. 2. Flux spectrum and the ISP-corrected polarisation degree P, Stokes Q and U parameters, and the polarisation angle θ for SN 2017gci at +3.3 d (left) and +29.0 d (right). The polarimetry data are binned to 25 Å in rest frame for visual clarity, but the flux spectra are shown at the natural binning of the spectrograph (~3.3 Å). The most notable line features (vertical lines) and telluric bands (grey regions) are highlighted. At +3.3 d, the polarisation degree increases towards the red, while at +29.0 d it is found at a consistently low value.

bright stars in our imaging polarimetry. As such, we only estimate the ISP of the Milky Way covered by the stars. We do not have the means to estimate the host galaxy ISP, but given that we retrieve consistently low level polarisation for all of our SNe (see Table B.7), the contribution from the respective host galaxies appears to be small. This is expected given that the host galaxies of SLSNe-I are typically found to be low mass (e.g. Neill et al. 2011; Lunnan et al. 2014; Leloudas et al. 2015b; Perley et al. 2016; Schulze et al. 2018).

The adopted ISPs are summarised in Table 2. For imaging polarimetry, the ISPs are vectorially subtracted from the obtained Stokes Q and U parameters. For the spectropolarimetry of SN 2017gci, the correction is performed using an empirical Serkowski law: $p(\lambda)/p_{\rm max} = \exp\left[-K \ln^2(\lambda_{\rm max}/\lambda)\right]$, where $p_{\rm max}$ is the maximum polarisation at wavelength $\lambda_{\rm max}$ (Serkowski et al. 1973). We used the V band ISP ($P_{\rm ISP} = 0.50\%$) and commonly used $\lambda_{\rm max} = 5500$ Å and $K = 1.15$ (Serkowski et al. 1975) for the correction. See Appendix A for details of the ISP estimation for individual SNe.

4. Polarimetry of SN 2017gci

In Fig. 2 we present flux spectra of SN 2017gci along the ISP-corrected P, Stokes Q and U parameters, and the polarisation angle θ as a function of wavelength for the VLT spectropolarimetry obtained at +3.3 d and +29.0 d. In both epochs, we see a low level of polarisation along most of the continuum spectrum. However, there is one notable difference: at +3.3 d the polarisation degree increases redward from $P \sim 0.1\% - 0.2\%$ at ~4000 Å to $P \sim 0.5\%$ at ~8000 Å, while at +29.0 d it is found at a constant level of $P \sim 0.1\%$ throughout the wavelength range.

The changes can also be seen in Fig. 3, where we present the Stokes $Q-U$ planes for the ISP-corrected spectropolarimetry. Such diagrams offer an intuitive visualisation of the polarimetric properties, as both P ($\sqrt{Q^2+U^2}$) and θ ($0.5 \arctan(U/Q)$) are directly related to the Stokes parameters. Following Maund et al. (2010), we use principal component analysis to define ellipses shown in red that encapsulate the spread of the data. The ellipses are drawn at the barycentre of the data ($\tilde{Q}$, $\tilde{U}$) and show the direction of the maximum variance at angle θ_d with respect to N/S axis on the sky ($\theta_d > 0°$ implies tilt towards east). The shape of the ellipses also quantifies the fraction of polarisation carried towards the dominant and orthogonal directions as the minor-over-major axial ratio (b/a). A ratio of $b/a = 0$ refers to the ideal situation where all polarisation is carried by the dominant direction. To guide the eye, we draw a 'dominant axis' in the direction of the maximum variance θ_d in dashed red. At +3.3 d, the data are off-centre and follow the dominant axis at $\theta_d \sim -40°$ with $b/a = 0.58$. However, at +29.0 d, the data spread is nearly circular ($b/a = 0.81$) and clustered around $P = 0\%$. While we show a dominant axis at $\theta_d \sim 25°$, the tendency of the data is significantly less prominent compared to +3.3 d. We also note that, as at the first epoch the dominant axis passes through $P = 0\%$

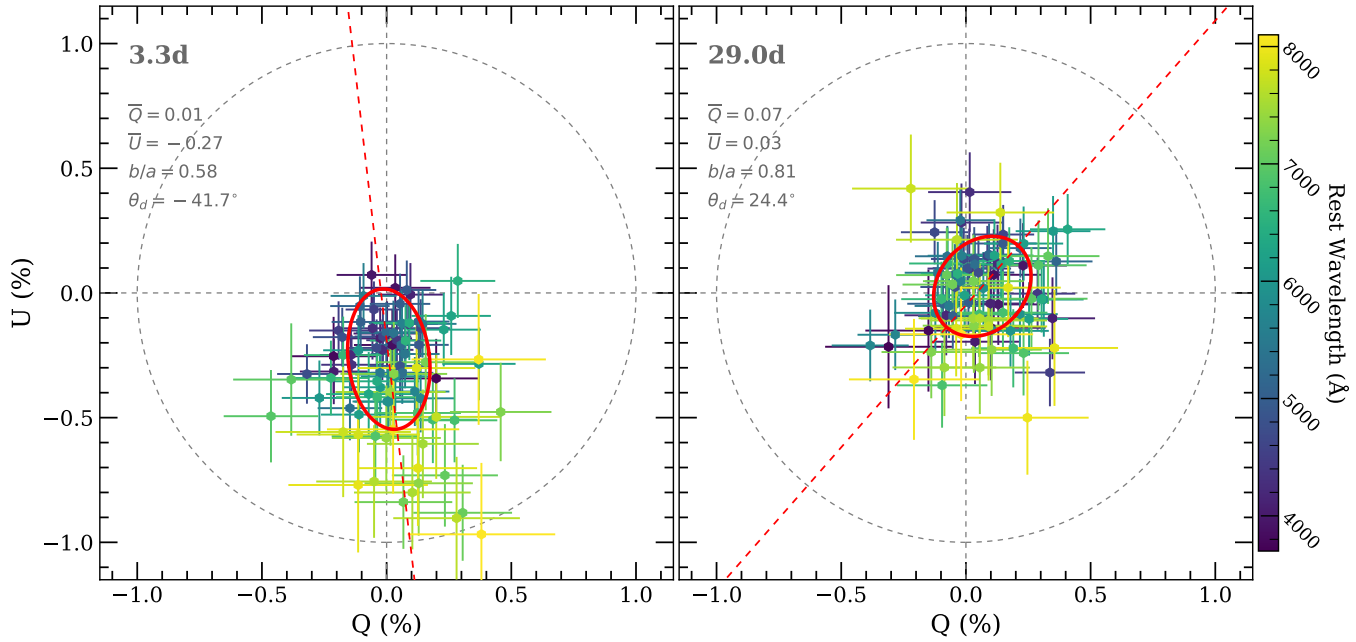

Fig. 3. $Q-U$ planes for the ISP-corrected spectropolarimetry of SN 2017gci at +3.3 d (left) and +29.0 d (right). The data colours follow wavelengths as indicated by the colour bar and the dashed grey lines mark $Q = 0$, $U = 0$, and $P = 1$. The red ellipses drawn at the barycentre of the data $(\tilde{Q}, \tilde{U})$ are based on a principal component analysis (Maund et al. 2010) and quantify the direction of the maximum variance of the polarisation (major axis) and the ratio of polarisation toward the orthogonal direction (the minor-to-major axis ratio b/a). The dominant axis (dashed red line) is drawn along the semi-major axis of the ellipse at an angle θ_d as measured from north towards east on the sky. At the first epoch, the data appear to follow the dominant axis within the observational noise, but at the second epoch the points are clustered roughly circularly around $P = 0$ with a weaker tendency along the drawn dominant axis.

and at the second epoch the data points are clustered around it, our estimate for the ISP appears to be correct.

A preferred orientation of data points on the Stokes $Q-U$ plane implies the presence of axial symmetry. Geometric deviation from spherical symmetry may be caused by three different mechanisms: (i) inherently aspherical photosphere (e.g. Höflich 1991), (ii) absorbing body covering only a part of the photosphere (e.g. Kasen et al. 2003), and (iii) an off-centre power source (e.g. Höflich 1995). Given that the low-level polarisation at +29.0 d implies spherical symmetry, option (iii) is unlikely the cause of the continuum polarisation at +3.0 d. Furthermore, Fiore et al. (2021) identified broad C II absorption lines in near-peak spectra of SN 2017gci. As shown in Fig. C.6, these lines do not project loops on the $Q-U$ plane – as was seen in SN 2018bsz (Pursiainen et al. 2022) – nor do they follow the drawn dominant axis as would be expected if the polarisation properties at +3.3 d were caused by an uneven distribution of absorbing material. Thus, option (ii) does not seem to be the cause of the tendency of the data and we assume that the polarisation is caused by an inherently aspherical photosphere. The photosphere is found at an angle of $\theta_d = -41.7°$ on the sky (i.e. westward from the N/S axis). For limiting polarisation of ∼0.5%, the lower limit of the physical axial ratio is $a/b \sim 1.1$ assuming an oblate ellipsoid (Höflich 1991). The data points appear to be mostly within the observational noise from the dominant axis, but we cannot rule out the possibility that some SN ejecta deviate from the discussed configuration, inducing polarisation to the orthogonal direction. A signature of such deviations are the loops in the $Q-U$ plane caused by the absorbing material (e.g. Wang & Wheeler 2008). While we did not identify such loops, the data over C II λ6580 appear to be tentatively orthogonal to the dominant axis but no such tendency is present in other lines (see Fig. C.6). This could indicate a deviation from the slightly spheroidal configuration. However, as the data over the line do not pass through $P = 0\%$, the position angle changes dramatically over the wavelength range implying that the absorbing body would have to have a complicated structure in front of the photosphere. At the second epoch, no clear loops are visible either. While only a weak tendency towards the dominant direction was seen in Fig. 3, Mg II λ4481 appears to be orthogonal to the dominant axis at $\theta_d \sim 25°$ while Na I λ5893 and tentatively C II λ6580 are along it. While the Na I λ5893 line is faint in the spectrum (see Fig. 2), it becomes stronger soon after, as shown by Fiore et al. (2021).

The two epochs of spectopolarimetry imply that the photosphere of SN 2017gci evolved from a slightly aspherical configuration to a more spherical one in the first month of its post-peak evolution. While the change appears to be modest, it is still surprising given that SLSNe-I are typically observed to either have a roughly constant geometry or become more aspherical with time, and such evolution has not been seen in the other three SLSNe-I with spectropolarimetry to date (SN 2015bn, SN 2017egm and SN 2018bsz). For SN 2015bn, the two epochs of VLT/FORS2 spectropolarimetry at −23.7 d and +27.5 d presented by Inserra et al. (2016) show an increasing polarisation degree (see also Leloudas et al. 2017). The data also show a strong wavelength dependence at both epochs. In the first epoch, the polarisation degree appears to increase towards the red (as in SN 2017gci) and at the second epochs towards the blue, following approximately the same dominant axis at both epochs. Based on Monte Carlo radiative-transfer modelling, Inserra et al. (2016) propose that the wavelength dependency can be a result of increasing depolarisation towards the blue caused by an increase in line opacity from red to blue. A

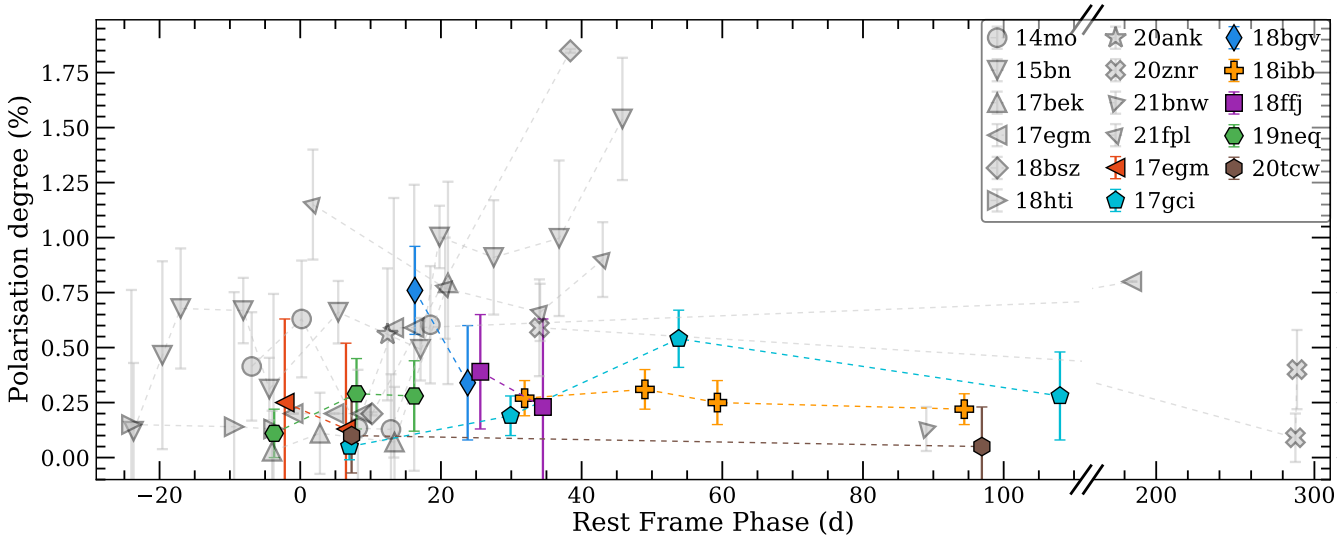

Fig. 4. Polarisation degree vs. rest-frame phase measured from the peak brightness in r/V band. The literature data collected from sources listed in Table 1 are shown with grey markers. The data are in V band (or comparable), apart from SN 2020znr (R). No ISP correction is performed for SN 2018bgv. For SN 2018hti, we performed the ISP correction based on values presented in Lee (2019) and for SN 2018bsz we assume the Case A ISP as presented by Pursiainen et al. (2022). We note the break and scale change in the x-axis at 150 d.

similar interpretation was made by Patat et al. (2012) to explain the blue-to-red increase of P seen in spectropolarimetry of the subluminous Type Ia SN 2005ke. For SN 2017egm, Bose et al. (2018) presented three epochs of spectropolarimetry at −1 d, +5 d, and +9 d and Saito et al. (2020) a fourth epoch at +185 d. The SN showed a low level of polarisation near the peak with no particular line features, but at +185 d the level of continuum polarisation had increased to ∼0.8%. Finally, for SN 2018bsz, the polarimetric evolution appears to be strongly affected by interaction with highly aspherical CSM (Pursiainen et al. 2022), and comparison to SN 2017gci is not fruitful.

While the spectropolarimetry shows a low level of polarisation at +29.0 d, the imaging polarimetry at ∼+55 d shows that the polarisation degree has increased to $P \sim 0.5\%$ in V band. In the $Q-U$ plane, the SN is found at $Q \sim -0.4\%$, $U \sim 0.4\%$ (see Fig. C.5), that is, in almost the opposite direction in comparison to +3.3 d. Assuming that the V band measurement represents the overall behaviour of the continuum polarisation, we find a position angle of $\theta \sim 70°$ at +55 d, indicating a rotation of ∼70° on the sky compared to +3.3 d. However, we note that the V band covers several notable emission lines (Fe II in particular; Fiore et al. 2021) that are possibly depolarising the signal and the inherent continuum polarisation might be higher.

Interestingly, the maximum of P coincides with two unusual observables discussed by Fiore et al. (2021): a 'knee' in the light curve and an appearance of a broad emission feature at 6520 Å that could be Hα and related to an interaction with CSM. Furthermore, Stevance & Eldridge (2021) used the stellar models made with the Binary Population And Spectral Synthesis (BPASS; Eldridge et al. 2008, 2017; Stanway & Eldridge 2018) code to investigate the progenitor properties, and concluded that the preferred progenitor, namely a 30 $M_\odot$ star in a binary system, can lose its hydrogen envelope via common envelope evolution, mass transfer in the binary system, and strong stellar winds just prior to the explosion, explaining the H-poor nature of the SN but also the possible detection of H-rich CSM. If these three observables are related to each other, this is evidence that the SN interacted with CSM, which affected its photometric, spectroscopic, and polarimetric evolution in a similar manner to SN 2018bsz (Pursiainen et al. 2022), and might indicate the presence of aspherical CSM. Finally, the last data point at ∼+108 d shows a tentative decrease in the polarisation degree (see Fig. 4). If real, this could signify the expected behaviour at late times when the SN is evolving towards the nebular phase. At this stage, the optical depth of electron scattering – and as a result the polarisation – decreases as is already seen in Type IIP SNe for example (e.g. Leonard et al. 2006; Chornock et al. 2010). However, due to the high uncertainty, it is unclear whether or not the decrease is real.

We also compared the spectral and imaging polarimetry taken at comparable epochs. We retrieved the broad-band values

Table 3. Details of the decline-rate analysis.

SN	Band	$\lambda_{\rm eff}$ (Å)	Rate (mag/100 d)	Stretch	Class
LSQ14mo	V	4389	5.62	6.03	Fast
SN 2015bn	g'	4236	1.73	1.86	Slow
PS17bek	r	4914	5.36	5.76	Fast
SN 2017egm	g	4660	1.98	2.13	Slow
SN 2017gci	g	4420	3.82	4.11	Slow
SN2018bgv	g	4453	7.36	7.91	Fast
SN 2018bsz	g	4680	1.67	1.80	Slow
SN 2018hti	g	4527	1.81	1.95	Slow
SN 2018ibb	V	4727	1.03	1.11	Slow
SN2019neq	g	4345	5.84	6.28	Fast
SN2020ank	c	4269	4.15	4.46	Fast
SN 2020tcw	g	4514	3.47	3.73	Slow
SN 2020znr	g	4368	0.93	1.00	Slow
SN 2021bnw	g	4376	1.66	1.79	Slow
SN 2021fpl	g	4309	3.02	3.25	Slow

Notes. The stretch refers to the decline rate compared to that of SN 2020znr. The SNe that decline faster than 4 mag/100 d are referred to as Fast.

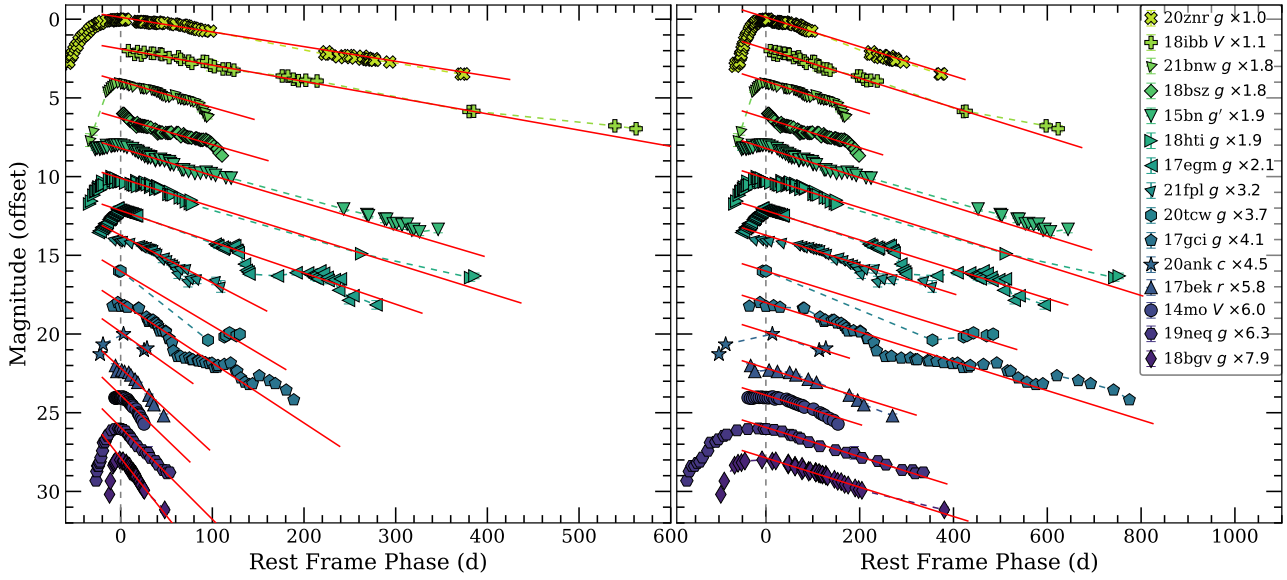

Fig. 5. Light curves used to estimate the decline rates (left) and the light curves stretched to the decline rate of SN 2020znr (right). The light curves are offset and the SNe are shown in the order from slow to fast for visual clarity. The multiplication factors used are given in the legend. The linear fits are shown with red lines. Only the data points after the dashed vertical grey line are used for the fits. We note that SN 2018ffj is excluded due to an uncertain peak epoch. The light curves are collected from the following sources: SN 2020znr, SN 2021fpl, SN 2020tcw, and SN 2019neq from ZTF via the Alerce broker (Förster et al. 2021), and SN 2018ibb (Schulze et al. 2023), SN 2018bsz (Chen et al. 2021), SN 2015bn (Nicholl et al. 2016b,a), SN 2018hti (Fiore et al. 2022), SN 2017egm (Bose et al. 2018; Hosseinzadeh et al. 2021), SN 2017gci (Fiore et al. 2021), SN 2020ank from ATLAS (Tonry et al. 2018), LSQ14mo (Leloudas et al. 2015a), SN2018bgv (Lunnan et al. 2020).

from the spectral polarimetry by integrating the individual o and e beam spectra over the VLT $V_{\rm HIGH}$ filter. The resulting Stokes parameters are:

– +3.3 d: $Q = 0.01 \pm 0.02\%$, $U = -0.20 \pm 0.02\%$,
– +29.0 d: $Q = 0.02 \pm 0.02\%$, $U = 0.09 \pm 0.02\%$.

Based on the imaging polarimetry, we find:

– +7.0 d: $Q = -0.05 \pm 0.06\%$, $U = -0.05 \pm 0.06\%$,
– +29.9 d: $Q = 0.06 \pm 0.09\%$, $U = 0.20 \pm 0.09\%$.

The second epoch of spectral polarimetry (+29.0 d) is consistent with imaging polarimetry taken the night after, but a minor difference is seen in the U of the spectral polarimetry taken at +3.3 d in comparison to +7.0 d. This possibly signifies short-timescale (∼4 d) variation, but could also be a consequence of different observational methods and reduction procedures. As such, we consider the imaging and spectral polarimetry to yield consistent results.

5. Evolution of polarisation for a sample of SLSNe-I

Figure 4 presents the evolution of polarisation degree as a function of the rest-frame phase for all SLSNe-I for which polarimetry is available. The seven SLSNe-I presented in this paper are highlighted with coloured markers, and the SNe found in the literature are shown in grey. For SN 2017egm, we show our data and literature data separately. As illustrated in the figure, we increase the number of SLSNe-I with any polarimetric observations significantly, but we also present data at epochs $\gtrsim$+100 d for two more SLSNe.

Considering the diverse light-curve-evolution timescales seen for SLSNe-I (see e.g. Nicholl et al. 2015), one-to-one comparison with respect to their peak times is not a reliable way to investigate the diversity of their polarimetric evolution. To account for this, we stretched the light curves so that they have a common decline rate using simple linear fits[1]. We chose SN 2020znr as the reference as it is the slowest declining SLSNe-I in the sample. The light curve bands were chosen so that their central wavelengths would be similar, allowing a meaningful comparison. The details of the fits are shown in Table 3 and the light curves before and after the stretch are presented in Fig. 5. There is clearly a large diversity in the sample, as the fastest declining SN in our sample (SN 2018bgv) declines 7.9 times faster than SN 2020znr.

In the literature, SLSNe-I have been divided into 'fast' and 'slow' subgroups based on their photometric and spectroscopic properties (see e.g. Inserra et al. 2018; Quimby et al. 2018). In general, photometrically slow SLSNe-I also evolve spectroscopically slower in comparison to the fast-evolving ones. However, there is no clear threshold to separate the two based on their photometric decline rates. For the purposes of this analysis, we refer to the SNe that decline at $\geq$4 mag/100 d as Fast SLSNe-I and the rest as Slow SLSNe-I. While the choice is arbitrary, it agrees well with prototypical events such as LSQ14mo (e.g. Chen et al. 2017; Leloudas et al. 2015a) and SN 2015bn (e.g. Nicholl et al. 2016b). Additionally, the classes of events such as SN 2020ank (Fast; Kumar et al. 2021) and SN 2017gci (Slow; Fiore et al. 2021) agree well with the Fast–Slow criteria of Inserra et al. (2018). In Fig. 6 (top), we present the polarisation degree as a function of normalised rest-frame phase, highlighting the Fast–Slow distinction. Only Slow SLSNe have shown a non-zero polarisation degree. However, there are only five Fast SLSNe and none of them were followed sufficiently late to conclude that they did not exhibit non-zero P, and indeed only SN 2018bgv has been observed after it declined $\gtrsim$1 mag from peak brightness. Given that the slow-evolving SN 2017gci showed increasing P only after this, it is not possible to conclude whether or not the Fast SLSNe inherently exhibit a non-zero polarisation degree.

Furthermore, Quimby et al. (2018) introduced the concept of spectroscopic phase for SLSNe-I. While it is beyond the means of this study to replicate their procedure, we inspected

[1] The fits were performed using `LMFIT` (Newville et al. 2014).

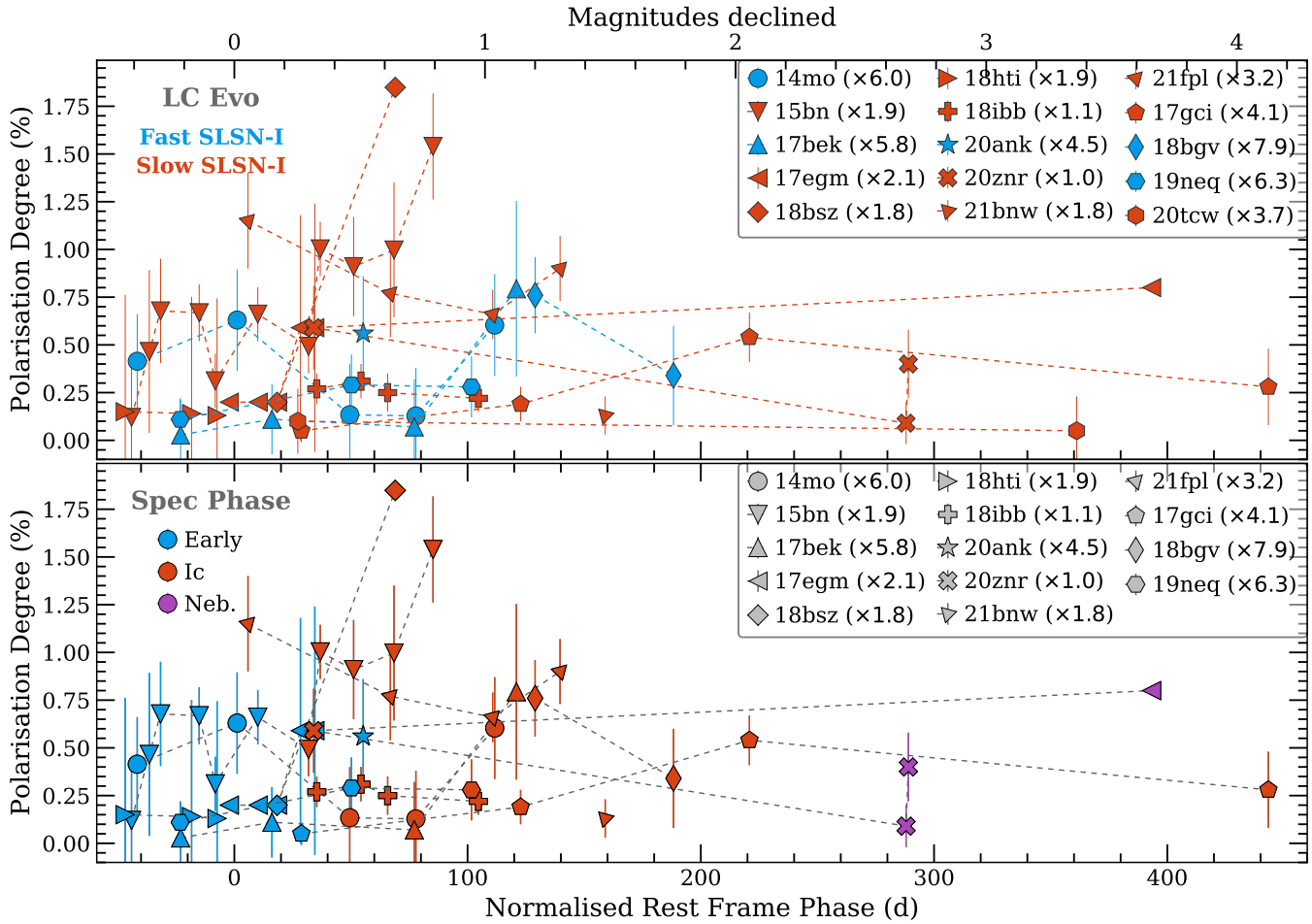

Fig. 6. Polarisation degree vs. the normalised rest frame phase for SLSNe-I with polarimetric data highlighting the diverse decline rates (top) and spectroscopic phase of each epoch of polarimetry (bottom). The stretch factors used to normalise the decline rates are shown in the legend. The top axis refers to the number of magnitudes declined by the SNe based on the linear fits. Only slowly evolving SLSNe-I have shown non-zero P, but the Fast ones have not been observed sufficiently late on in their evolution to rule it out. Spectroscopically, the SLSNe-I exhibit low polarisation during the Early phase, but no relation to polarimetry can be identified at the later phases. We note that SN 2018ffj is not shown due to the unconstrained peak time and SN 2020tcw is not shown in the bottom panel due to uncertain spectroscopic phases during the polarimetric epochs.

the spectral phase during which the polarimetric observations were obtained and divided them into three approximate categories: (1) the 'Early phase' spectra consist of hot, blue continua that show mostly O II absorption lines and/or C II P Cygni profiles; (2) the 'Ic phase' spectra are dominated by the elements seen in Type Ic SNe during the photospheric phase (e.g. Mg, Ca, O, Fe); and (3) 'Pseudo-nebular' spectra are in general similar to nebular phase spectra of Type Ic SNe and show prominent forbidden emission lines (e.g. [Ca II]). The spectroscopic phases are highlighted in Fig. 6 (bottom). No SLSNe-I show significant polarisation during the Early phase, directly implying that the outermost layers of SLSNe-I are consistently spherical, or at least almost spherical. While the spectral transition between Early and Ic phases results in an increase in polarisation for some events (e.g. SN 2015bn), this does not appear to be the case for all (e.g. LSQ14mo). Finally, pseudo-nebular phase polarimetry has been obtained only for two SLSNe-I: SN 2020znr does not show increasing polarisation, but SN 2017egm does. Therefore, we conclude that the SLSNe-I exhibit low polarisation during the Early phase, but no relation between polarimetric properties and the spectroscopic phases were identified at the later phases.

Given that the sample of SLSNe-I with polarimetry at late times is still small, it is not necessarily surprising that no strong tendencies were identified. One possibly important factor – which we cannot properly investigate due to the small sample especially at the late times – is the effect of the viewing angle. The observed polarisation degree of a SN is effectively dictated by how circular the projection of the photosphere appears to be on the sky. While a small polarisation degree will always be obtained for an unobstructed spherical photosphere, an inherently aspherical one might result in a high or low value depending on the angle. As such, the diversity of P shown in Fig. 6 could at least partially be caused by the distribution of the viewing angles. However, it is interesting to note that comparable or even smaller samples of other types of SNe have lead to strong conclusions on their nature. For instance, Chornock et al. (2010) showed that a sample of five Type IIP SNe was sufficient to verify that while the SNe have nearly spherical hydrogen envelopes (i.e. low P), their inner cores are highly aspherical. Therefore, the diversity of the polarisation properties of SLSNe-I might imply that the distribution of their photospheric shapes with time is inherently diverse.

Not only are the SLSNe-I with non-zero polarisation degree all slowly evolving, the four SNe that show increasing P at some stage have all been reported to exhibit some manner of undulation or break during the light-curve decline, while the other SLSNe-I with multi-epoch polarimetry show smooth photometric

evolution (see Fig. 5). These four SNe are SN 2015bn (Nicholl et al. 2016b), SN 2017egm (Hosseinzadeh et al. 2021), SN 2017gci (Fiore et al. 2021), and SN 2018bsz (Chen et al. 2021). While there are a few 'borderline' cases where the topic is difficult to investigate because of poorly sampled polarimetric data (SN 2020tcw and SN 2021bnw) or unclear polarimetric evolution (SN 2021fpl), this implies that the irregular light-curve evolution and the increasing polarisation degree are related.

The irregular light curves have been a topic of discussion in the literature. In particular, Hosseinzadeh et al. (2021) and Chen et al. (2023b) investigated the prevalence of undulations during the light-curve decline in SLSNe-I. While both authors concluded that they are common, they could not determine whether they are caused by CSM interaction or by a magnetar engine via an increase in energy input or a sudden decrease in the ejecta opacity. For SN 2018bsz, Pursiainen et al. (2022) showed that the polarisation properties changed drastically after the CSM-related multi-component Hα emission line appeared at $\sim$+30 d. The light curve also entered a pseudo-plateau phase roughly at the same time, lasting until $\sim$+100 d when one of the Hα components suddenly faded. These latter authors concluded that both the polarisation properties and the light-curve evolution were strongly affected by interaction with close-by, highly aspherical CSM that was enshrouded by the SN ejecta after the explosion and re-emerged only when the photosphere had sufficiently receded. For SN 2017gci, Fiore et al. (2021) discuss the possibility that a broad spectral feature at 6520 Å – which appeared at the same time as a knee in the light curve ($\sim$+50 d) – is Hα emission arising from CSM. Given that we report an increase in polarisation degree at a similar phase ($\sim$55 d), these observables are likely related and caused by the CSM interaction. On the other hand, the dense spectroscopic coverage of SN 2015bn (Nicholl et al. 2016a,b) and SN 2017egm (Nicholl et al. 2017; Bose et al. 2018) does not reveal any obvious lines attributed to CSM interaction. However, Wheeler et al. (2017) model the bolometric light curve of SN 2017egm up to $\sim$+30 d (i.e. before the light-curve undulations) and argue that CSM interaction models can account for the sharp peak seen in the light curve, whereas the magnetar models have difficulty explaining it. Unfortunately, the sparse polarimetric data of SN 2017egm do not allow an investigation into whether the change in polarisation occurred at the same time as the light-curve undulations, but for SN 2015bn, the maximum polarisation is measured during a knee in the light curve. In summary, increasing polarisation degree and irregular light-curve evolution appear to be related and in up to two out of four SLSNe-I with increasing P, photometric, spectroscopic and polarimetric properties are affected by CSM interaction. Therefore, we conclude that CSM interaction plays a key role in understanding the polarimetric evolution of SLSNe-I.

Finally, we emphasise that the number of SLSNe-I with crucial late-time polarimetry is still very small. As shown in Fig. 6, only three SNe have been observed after they have declined more than 2 mag. Based on Fig. 6, the spectra start to evolve towards the nebular phase only after this. As the photospheres recede over time, multi-epoch polarimetry from early times to such late phases are needed to map out the degree of asphericity at different layers of the ejecta, therefore providing a more comprehensive picture of the geometry of SLSNe-I. Therefore, to investigate the true diversity of their polarimetric evolution and to test the different models for the underlying energy source, well-cadenced observations have to be obtained for more SLSNe-I both with and without irregular light-curve evolution.

6. Conclusions

We present linear polarimetry for seven hydrogen-poor superluminous supernovae (SLSNe-I) of which only one has previously published polarimetric data. This is the largest dataset presented to date and increases the number of SLSNe-I with polarimetry in the literature by 60%. The best-studied event is SN 2017gci, for which we present two epochs of spectropolarimetry – which has only previously been obtained for three SLSNe-I – along with further imaging polarimetry with VLT/FORS2. Using our data set and all available data in the literature, we also present a sample analysis of SLSN-I polarimetry.

The analysis of SN 2017gci reveals that it is the first SLSN-I for which a decrease in polarisation degree has been observed. In the first epoch of spectropolarimetry at +3.3 d, the data are off-centre on the $Q-U$ plane and follow a dominant axis – indicative of axial symmetry. Assuming an oblate photosphere, $P \lesssim 0.5\%$ indicates an aspherical configuration with a physical axial ratio of $a/b \lesssim 1.1$ (Höflich 1991) if viewed equator-on. The polarisation degree increases from blue to red, which in the literature has been attributed to increasing line opacity towards the blue (e.g. Patat et al. 2012; Inserra et al. 2016). The spectropolarimetry at +29.0 d shows that the data are clustered around $P = 0\%$ on the $Q-U$ plane, implying that the photosphere of SN 2017gci became more spherical in the first month post-peak. The later imaging polarimetry shows that the polarisation degree increased again reaching a maximum of $P \sim 0.5\%$ at $\sim$+55 d, but towards a different direction on the $Q-U$ plane, indicating a rotation of $\sim$70° on the sky in comparison to +3.3 d. The rotation might be related to CSM interaction, as already implied by a simultaneous 'knee' in the light curve and the possible detection of broad Hα emission (Fiore et al. 2021).

Furthermore, we examined whether the polarimetric properties of SLSNe-I showed any relations with their photometric and spectroscopic properties. After normalising the light curves for the diverse decline rates, the polarimetry showed no clear relation with the photometric evolution timescale. While only Slow SLSNe-I have been found to show a non-zero polarisation degree, the fast-evolving ones have not been observed at sufficiently late times to conclude that none of them show increasing P. Furthermore, the spectroscopic phases of the polarimetric epochs appear to have only a small effect. While the polarimetry taken during early spectroscopic phases (i.e. dominated by blue continuum) shows low polarisation – indicative of high spherical symmetry –, no clear correlation between the polarimetric and spectroscopic evolution was seen at later epochs when the SNe were spectroscopically similar to Type Ic SNe during the photospheric or nebular phases.

We report that the four SLSNe-I that have shown increasing polarisation degree to date (SN 2015bn, SN 2017egm, SN 2017gci, and SN 2018bsz) also exhibit irregular light-curve declines, while the other SLSNe-I with multi-epoch polarimetry show smooth photometric evolution. Given that CSM interaction affected the spectroscopic, photometric, and polarimetric properties of up to half of the four SNe, we conclude that the CSM interaction clearly plays an important role in understanding the polarimetric evolution of SLSNe-I. However, due to the small number of SLSNe-I with well-cadenced polarimetry up to late times, the effect of a possible internal engine cannot be properly investigated. More SLSNe-I, both with and without light curve undulations, need to be followed with polarimetry from near-peak to late times in order to probe the intrinsic diversity of the geometric structure of their ejecta.

Acknowledgements. We thank the anonymous referee for the helpful feedback. M.P and G.L. are supported by a research grant (19054) from VILLUM FONDEN. A.C. is supported by NOIRLab, which is managed by the Association of Universities for Research in Astronomy (AURA) under a cooperative agreement with the National Science Foundation. M.B. acknowledges support from the European Union's Horizon 2020 Programme under the AHEAD2020 project (grant agreement n. 871158). S.S. acknowledges support from the G.R.E.A.T. research environment, funded by Vetenskapsrådet, the Swedish Research Council, project number 2016-06012. The research of Y.Y. is supported through a Bengier-Winslow-Robertson Fellowship. MN and AA are supported by the European Research Council (ERC) under the European Union's Horizon 2020 research and innovation programme (grant agreement No. 948381) and MN also by a Fellowship from the Alan Turing Institute. AGY's research is supported by the EU via ERC grant No. 725161, the ISF GW excellence center, an IMOS space infrastructure grant and a GIF grant, as well as the André Deloro Institute for Advanced Research in Space and Optics, The Helen Kimmel Center for Planetary Science, the Schwartz/Reisman Collaborative Science Program and the Norman E Alexander Family M Foundation ULTRASAT Data Center Fund, Minerva and Yeda-Sela; AGY is the incumbent of the Arlyn Imberman Professorial Chair. This work is based (in part) on observations collected at the European Organisation for Astronomical Research in the Southern Hemisphere under ESO programmes 099.D-0169(A) and 0100.D-0209(A) and on observations made with the Nordic Optical Telescope, owned in collaboration by the University of Turku and Aarhus University, and operated jointly by Aarhus University, the University of Turku and the University of Oslo, representing Denmark, Finland and Norway, the University of Iceland and Stockholm University at the Observatorio del Roque de los Muchachos, La Palma, Spain, of the Instituto de Astrofisica de Canarias under NOT programmes 57-010, 58-005, 59-013, 60-027, 62-003, 63-006. The NOT data presented here were obtained with ALFOSC, which is provided by the Instituto de Astrofisica de Andalucia (IAA) under a joint agreement with the University of Copenhagen and NOT. This work benefited from L.A.Cosmic (van Dokkum 2001), IRAF (Tody 1986), PyRAF and PyFITS. PyRAF and PyFITS are products of the Space Telescope Science Institute, which is operated by AURA for NASA. We thank the authors for making their tools and services publicly available.

References

Anderson, J. P., Pessi, P. J., Dessart, L., et al. 2018, A&A, 620, A67
Angus, C. R., Smith, M., Sullivan, M., et al. 2019, MNRAS, 487, 2215
Appenzeller, I., Fricke, K., Fürtig, W., et al. 1998, The Messenger, 94, 1
Bertin, E., & Arnouts, S. 1996, A&AS, 117, 393
Bose, S., Dong, S., Pastorello, A., et al. 2018, ApJ, 853, 57
Chen, T. W., Nicholl, M., Smartt, S. J., et al. 2017, A&A, 602, A9
Chen, T. W., Brennan, S. J., Wesson, R., et al. 2021, ArXiv e-prints [arXiv:2109.07942]
Chen, Z. H., Yan, L., Kangas, T., et al. 2023a, ApJ, 943, 41
Chen, Z. H., Yan, L., Kangas, T., et al. 2023b, ApJ, 943, 42
Chevalier, R. A., & Irwin, C. M. 2011, ApJ, 729, L6
Chomiuk, L., Chornock, R., Soderberg, A. M., et al. 2011, ApJ, 743, 2
Chornock, R., Filippenko, A. V., Li, W., & Silverman, J. M. 2010, ApJ, 713, 1363
Cikota, A., Patat, F., Cikota, S., & Faran, T. 2017, MNRAS, 464, 4146
Cikota, A., Leloudas, G., Bulla, M., et al. 2018, MNRAS, 479, 4984
Cikota, A., Patat, F., Wang, L., et al. 2019, MNRAS, 490, 578
De Cia, A., Gal-Yam, A., Rubin, A., et al. 2018, ApJ, 860, 100
Eldridge, J. J., Izzard, R. G., & Tout, C. A. 2008, MNRAS, 384, 1109
Eldridge, J. J., Stanway, E. R., Xiao, L., et al. 2017, PASA, 34, e058
Fiore, A., Chen, T. W., Jerkstrand, A., et al. 2021, MNRAS, 502, 2120
Fiore, A., Benetti, S., Nicholl, M., et al. 2022, MNRAS, 512, 4484
Förster, F., Cabrera-Vives, G., Castillo-Navarrete, E., et al. 2021, AJ, 161, 242
Gaia Collaboration (Vallenari, A., et al.) 2023, A&A, in press, https://doi.org/10.1051/0004-6361/202243940
Gal-Yam, A. 2012, Science, 337, 927
Gal-Yam, A. 2019, ARA&A, 57, 305
Gal-Yam, A., Mazzali, P., Ofek, E. O., et al. 2009, Nature, 462, 624
Heiles, C. 2000, AJ, 119, 923
Höflich, P. 1991, A&A, 246, 481
Höflich, P. 1995, ApJ, 440, 821
Hosseinzadeh, G., Berger, E., Metzger, B. D., et al. 2021, ApJ, 933, 14
Inserra, C., Bulla, M., Sim, S. A., & Smartt, S. J. 2016, ApJ, 831, 79
Inserra, C., Prajs, S., Gutierrez, C. P., et al. 2018, ApJ, 854, 175
Kasen, D., & Bildsten, L. 2010, ApJ, 717, 245
Kasen, D., Nugent, P., Wang, L., et al. 2003, ApJ, 593, 788
Kumar, A., Kumar, B., Pandey, S. B., et al. 2021, MNRAS, 502, 1678
Lee, C.-H. 2019, ApJ, 875, 121
Lee, C.-H. 2020, Astron. Nachr., 341, 651
Leloudas, G., Patat, F., Maund, J. R., et al. 2015a, ApJ, 815, L10
Leloudas, G., Schulze, S., Krühler, T., et al. 2015b, MNRAS, 449, 917
Leloudas, G., Maund, J. R., Gal-Yam, A., et al. 2017, ApJ, 837, L14
Leloudas, G., Bulla, M., Cikota, A., et al. 2022, Nat. Astron., 6, 1193
Leonard, D. C., Filippenko, A. V., Ganeshalingam, M., et al. 2006, Nature, 440, 505
Lunnan, R., Chornock, R., Berger, E., et al. 2014, ApJ, 787, 138
Lunnan, R., Fransson, C., Vreeswijk, P. M., et al. 2018, Nat. Astron., 2, 887
Lunnan, R., Yan, L., Perley, D. A., et al. 2020, ApJ, 901, 61
Maund, J. R., Craig Wheeler, J., Wang, L., et al. 2010, ApJ, 722, 1162
Maund, J. R., Steele, I., Jermak, H., Wheeler, J. C., & Wiersema, K. 2019, MNRAS, 482, 4057
Maund, J. R., Yang, Y., Steele, I. A., et al. 2021, MNRAS, 503, 312
Moriya, T. J., Sorokina, E. I., & Chevalier, R. A. 2018, Space Sci. Rev., 214, 59
Neill, J. D., Sullivan, M., Gal-Yam, A., et al. 2011, ApJ, 727, 15
Newville, M., Ingargiola, A., Stensitzki, T., & Allen, D. B. 2014, https://doi.org/10.5281/Zenodo.11813
Nicholl, M. 2021, Astron. Geophys., 62, 534
Nicholl, M., Smartt, S. J., Jerkstrand, A., et al. 2015, MNRAS, 452, 3869
Nicholl, M., Berger, E., Margutti, R., et al. 2016a, ApJ, 828, L18
Nicholl, M., Berger, E., Smartt, S. J., et al. 2016b, ApJ, 826, 39
Nicholl, M., Berger, E., Margutti, R., et al. 2017, ApJ, 845, L8
Pastorello, A., Smartt, S. J., Botticella, M. T., et al. 2010, ApJ, 724, L16
Patat, F. 2017, Handbook of Supernovae (Cham: Springer International Publishing), 1017
Patat, F., Höflich, P., Baade, D., et al. 2012, A&A, 545, A7
Perley, D. A., Quimby, R. M., Yan, L., et al. 2016, ApJ, 830, 13
Plaszczynski, S., Montier, L., Levrier, F., & Tristram, M. 2014, MNRAS, 439, 4048
Poidevin, F., Omand, C. M., Perez-Fournon, I., et al. 2022, MNRAS, 511, 5948
Poidevin, F., Omand, C. M. B., Könyves-Tóth, R., et al. 2023, MNRAS, 521, 5418
Pursiainen, M., Leloudas, G., Paraskeva, E., et al. 2022, A&A, 666, A30
Quimby, R. M., Aldering, G., Wheeler, J. C., et al. 2007, ApJ, 668, L99
Quimby, R. M., Kulkarni, S. R., Kasliwal, M. M., et al. 2011, Nature, 474, 487
Quimby, R. M., Cia, A. D., Gal-Yam, A., et al. 2018, ApJ, 855, 2
Saito, S., Tanaka, M., Moriya, T. J., et al. 2020, ApJ, 894, 154
Schulze, S., Krühler, T., Leloudas, G., et al. 2018, MNRAS, 473, 1258
Schulze, S., Fransson, C., Kozyreva, A., et al. 2023, A&A, submitted [arXiv:2305.05796]
Serkowski, K. 1973, in Interstellar Dust Relat. Top., eds. J. M. Greenberg, & H. C. van de Hulst, IAU Symp., 52, 145
Serkowski, K., Mathewson, D. L., & Ford, V. L. 1975, ApJ, 196, 261
Shapiro, P. R., & Sutherland, P. G. 1982, ApJ, 263, 902
Simmons, J. F. L., & Stewart, B. G. 1985, A&A, 142, 100
Soker, N. 2022, Res. Astron. Astrophys., 22
Soker, N., & Gilkis, A. 2017, ApJ, 851, 95
Stanway, E. R., & Eldridge, J. J. 2018, MNRAS, 479, 75
Stetson, P. B. 1987, PASP, 99, 191
Stevance, H. F., & Eldridge, J. J. 2021, MNRAS, 504, L51
Stevance, H. F., Maund, J. R., Baade, D., et al. 2019, MNRAS, 485, 102
Stevance, H. F., Baade, D., Bruten, J. R., et al. 2020, MNRAS, 494, 885
Tody, D. 1986, Instrum. Astron. VI, 0627, 733
Tonry, J. L., Denneau, L., Heinze, A. N., et al. 2018, PASP, 130, 988
Tran, H. D. 1995, ApJ, 440, 565
van Dokkum, P. G. 2001, PASP, 113, 1420
Wang, L., & Wheeler, J. C. 2008, ARA&A, 46, 433
Wang, L., Wheeler, J. C., & Höflich, P. 1997, ApJ, 476, L27
Wheeler, J. C., Chatzopoulos, E., Vinkó, J., & Tuminello, R. 2017, ApJ, 851, L14
Woosley, S. E. 2010, ApJ, 719, L204
Yan, L., Quimby, R., Ofek, E., et al. 2015, ApJ, 814, 108
Yan, L., Lunnan, R., Perley, D. A., et al. 2017, ApJ, 848, 6

Appendix A: ISP estimation

A.1. SN 2017egm

As shown in Figure C.1, there is no star in the FOV with which to reliably reduce the ISP from our data. Therefore, we adopt the ISP of Saito et al. (2020) ($Q_{\rm ISP} = 0.29 \pm 0.34\%$ and $U_{\rm ISP} = -0.40 \pm 0.3\%$) estimated based on the intrinsically unpolarised Ca II NIR triplet emission present in the pseudo-nebular phase spectropolarimetry.

A.2. SN 2017gci

We estimated the ISP for SN 2017gci using the numerous point sources in the VLT/FORS2 broad-band polarimetry. We used the three epochs with more than one cycle (set of observations over the four HWP angles) in order to exclude outliers. We set a strict S/N cut of 300 in every image to ensure accurate ISP caused by Galactic dust. First we estimated the ISP independently for each epoch by excluding measurements of stars that were not consistent between the cycles. For epochs one and three with two cycles, the field stars that have Stokes parameters that differ by $> 1\sigma$ were excluded, while for epoch four, which has three cycles, the remaining consistent measurements (if they existed) were kept. The ISP level for each epoch was determined using the error-weighted mean Stokes parameters and the final ISP by calculating the error-weighted average values among the three epochs of observations. Table A.1 summarises the ISPs estimated for SN 2017gci and we show the stars passing our criteria on the $Q-U$ plane in Figure C.2. We note that we also show the results for epoch two, with only one cycle of observations, for which the ISP was estimated based on all the field stars that passed the S/N cut. The large deviation in U is likely to be caused by variations of the observing condition during the exposure, which cannot be cross-checked using multiple cycles of observations because only one set of polarimetry was obtained. We also verified that the used stars are sufficiently far away to fully probe the Milky Way dust content. Following Tran (1995), a star needs to be ~150 pc above the Galactic plane to provide a good estimate for the Galactic ISP. Using the astrometric solutions from *Gaia* Data Release 3 (Gaia Collaboration et al. 2023), we conclude that all the stars are found above the threshold and thus should yield reliable results.

A.3. SN 2018bgv

We identify no bright point source in the FOV of the NOT/ALFOSC imaging polarimetry of SN 2018bgv. (see Figure C.1). Instead, we refer to the polarisation standard stars published in Heiles (2000) that are close to the location of SN 2018bgv. There are two stars within 2° of the SN and a further two within 5°, and the polarisation levels published for all these four stars are consistent with zero. Therefore, we adopt $Q_{\rm ISP} = 0.0\%$ and $U_{\rm ISP} = 0.0\%$.

Table A.1. Estimated ISPs for the individual epochs of VLT/FORS2 imaging polarimetry of SN 2017gci with the number of cycles per epoch (n). We note that the second epoch is based on one cycle of observation making it less reliable than the other three and was therefore excluded when estimating the final value.

Date	n	$Q_{\rm ISP}$ (%)	$U_{\rm ISP}$ (%)	$P_{\rm ISP}$ (%)
2017-08-29	2	-0.54 ± 0.02	-0.01 ± 0.02	0.54 ± 0.02
2017-09-23	1	-0.52 ± 0.03	-0.23 ± 0.03	0.57 ± 0.03
2017-10-19	2	-0.48 ± 0.02	-0.05 ± 0.02	0.48 ± 0.02
2017-12-17	3	-0.50 ± 0.02	-0.01 ± 0.02	0.50 ± 0.02
Final	-	-0.50 ± 0.01	-0.02 ± 0.01	0.50 ± 0.01

A.4. SN 2018ffj

For SN 2018ffj, there is one bright star in the NOT/ALFOSC FOV (see Figure C.1) adequate to estimate the ISP. After excluding the first epoch due to high lunar illumination (see Section 2.2), we find $Q_{\rm ISP} = 0.09 \pm 0.02\%$ and $U_{\rm ISP} = -0.08 \pm 0.02\%$. The comparison with the Heiles catalogue shows that this estimate is reasonable: seven out of ten stars within 4° of the SN have been measured to be unpolarised, while the remaining three exhibit low levels of polarisation, indicating that the Galactic ISP is less than ~0.15% near the SN line of sight. The star also fully probes the Galactic dust column. It is found at a Galactic latitude $b = -65.03°$ and parallax $p = 0.56$ mas corresponding position ~1600 pc above the Galactic plane.

A.5. SN 2019neq

For SN 2019neq, there are two bright point sources in the NOT/ALFOSC FOV (see Figure C.1). The e beam of Star 1 is found on the edge of the o beam image and the polarisation measurements may not be reliable. Star 2 was saturated in the first epoch of observation, and the second epoch of observation is contaminated by the bright moon. Therefore, we estimate the Galactic ISP based on the observations of Star 2 at epochs three and four. We find $Q_{\rm ISP} = 0.27 \pm 0.03\%$ $U_{\rm ISP} = -0.18 \pm 0.03\%$, which is consistent with the polarisation of $P_{\rm ISP} = 0.18 \pm 0.20\%$ of an unpolarised star within 3° from the location of the SN. The star is found at 650 pc above the Galactic plane ($b = 28.91°$ and $p = 0.74$ mas) and should probe the dust column sufficiently.

A.6. SN 2020tcw

For SN 2020tcw there are two bright stars in the ALFOSC FOV (see Figure C.1). Star 2 is in close proximity to the other, fainter targets, which may contaminate the measurements. Therefore, we use Star 1 and estimate the Galactic ISP to be $Q_{\rm ISP} = -0.16 \pm 0.11\%$ $U_{\rm ISP} = -0.03 \pm 0.11\%$. The low Galactic ISP estimated for SN 2020tcw is consistent with the zero-level polarisation towards the unpolarised stars within $2° - 4°$ of the location of the SN. The star is also located at a distance of 480 pc from the Galactic plane (latitude $b = 55.23°$ and $p = 1.71$ mas) and should provide a reliable estimate for the Galactic ISP.

Appendix B: Tables

Table B.1. Observations log for SN 2017gci in the spectropolarimetry (PMOS) and broad-band polarimetry (IPOL) modes.

Date and time (UTC)	Mode	Filter	HWP angle (°)	Exposure (s)	Seeing (")
2017-08-25 08:39:01	PMOS	free	0.0	750	0.77
2017-08-25 08:52:25	PMOS	free	45.0	750	1.1
2017-08-25 09:05:40	PMOS	free	22.5	750	1.21
2017-08-25 09:19:04	PMOS	free	67.5	750	1.06
2017-08-26 08:30:16	PMOS	free	0.0	750	0.75
2017-08-26 08:43:40	PMOS	free	45.0	750	0.88
2017-08-26 08:56:55	PMOS	free	22.5	750	0.98
2017-08-26 09:10:18	PMOS	free	67.5	750	0.91
2017-08-29 09:31:51	IPOL	$V_{\rm HIGH}$	0.0	80	0.55
2017-08-29 09:33:53	IPOL	$V_{\rm HIGH}$	45.0	80	0.5
2017-08-29 09:35:49	IPOL	$V_{\rm HIGH}$	22.5	80	0.47
2017-08-29 09:37:52	IPOL	$V_{\rm HIGH}$	67.5	80	0.47
2017-08-29 09:46:32	IPOL	$V_{\rm HIGH}$	0.0	80	0.5
2017-08-29 09:48:36	IPOL	$V_{\rm HIGH}$	45.0	80	0.53
2017-08-29 09:50:31	IPOL	$V_{\rm HIGH}$	22.5	80	0.51
2017-08-29 09:52:34	IPOL	$V_{\rm HIGH}$	67.5	80	0.52
2017-09-22 07:15:51	PMOS	free	0.0	900	0.94
2017-09-22 07:31:44	PMOS	free	45.0	900	0.67
2017-09-22 07:47:29	PMOS	free	22.5	900	0.7
2017-09-22 08:03:23	PMOS	free	67.5	900	0.82
2017-09-22 08:21:44	PMOS	free	0.0	900	0.86
2017-09-22 08:37:38	PMOS	free	45.0	900	0.8
2017-09-22 08:53:24	PMOS	free	22.5	900	0.77
2017-09-22 09:09:18	PMOS	free	67.5	900	0.61
2017-09-23 08:16:55	IPOL	$V_{\rm HIGH}$	0.0	140	0.69
2017-09-23 08:19:58	IPOL	$V_{\rm HIGH}$	45.0	140	0.65
2017-09-23 08:22:53	IPOL	$V_{\rm HIGH}$	22.5	140	0.68
2017-09-23 08:25:56	IPOL	$V_{\rm HIGH}$	67.5	140	0.68
2017-10-19 07:14:19	IPOL	$V_{\rm HIGH}$	0.0	120	0.57
2017-10-19 07:17:03	IPOL	$V_{\rm HIGH}$	45.0	150	0.56
2017-10-19 07:20:09	IPOL	$V_{\rm HIGH}$	22.5	150	0.6
2017-10-19 07:23:22	IPOL	$V_{\rm HIGH}$	67.5	150	0.58
2017-10-19 07:27:32	IPOL	$V_{\rm HIGH}$	0.0	150	0.6
2017-10-19 07:30:46	IPOL	$V_{\rm HIGH}$	45.0	150	0.66
2017-10-19 07:33:51	IPOL	$V_{\rm HIGH}$	22.5	150	0.68
2017-10-19 07:37:03	IPOL	$V_{\rm HIGH}$	67.5	150	0.61
2017-12-17 03:34:35	IPOL	$V_{\rm HIGH}$	0.0	400	0.72
2017-12-17 03:41:58	IPOL	$V_{\rm HIGH}$	45.0	400	0.74
2017-12-17 03:49:13	IPOL	$V_{\rm HIGH}$	22.5	400	0.87
2017-12-17 03:56:35	IPOL	$V_{\rm HIGH}$	67.5	400	0.73
2017-12-17 04:04:41	IPOL	$V_{\rm HIGH}$	0.0	400	0.8
2017-12-17 04:12:03	IPOL	$V_{\rm HIGH}$	45.0	400	0.74
2017-12-17 04:19:18	IPOL	$V_{\rm HIGH}$	22.5	400	0.58
2017-12-17 04:26:41	IPOL	$V_{\rm HIGH}$	67.5	400	0.52
2017-12-17 04:34:42	IPOL	$V_{\rm HIGH}$	0.0	400	0.52
2017-12-17 04:42:04	IPOL	$V_{\rm HIGH}$	45.0	400	0.51
2017-12-17 04:49:20	IPOL	$V_{\rm HIGH}$	22.5	400	0.51
2017-12-17 04:56:43	IPOL	$V_{\rm HIGH}$	67.5	400	0.52

Table B.2. Observations log for SN 2017egm.

Date and time (UTC)	Filter	HWP angle (°)	Exposure (s)
2017-06-17 22:00:05	R	0.0	40
2017-06-17 22:00:55	R	22.5	40
2017-06-17 22:01:44	R	45.0	40
2017-06-17 22:02:34	R	67.5	40
2017-06-19 22:02:06	V	0.0	40
2017-06-19 22:02:56	V	22.5	40
2017-06-19 22:03:45	V	45.0	40
2017-06-19 22:04:34	V	67.5	40
2017-06-19 22:06:18	R	0.0	40
2017-06-19 22:07:08	R	22.5	40
2017-06-19 22:07:58	R	45.0	40
2017-06-19 22:08:47	R	67.5	40
2017-06-19 22:10:16	I	0.0	40
2017-06-19 22:11:06	I	22.5	40
2017-06-19 22:11:55	I	45.0	40
2017-06-19 22:12:44	I	67.5	40
2017-06-28 22:40:41	V	0.0	40
2017-06-28 22:41:30	V	22.5	40
2017-06-28 22:42:20	V	45.0	40
2017-06-28 22:43:10	V	67.5	40
2017-06-28 22:44:29	R	0.0	40
2017-06-28 22:45:19	R	22.5	40
2017-06-28 22:46:07	R	45.0	40
2017-06-28 22:46:57	R	67.5	40
2017-06-28 22:48:18	I	0.0	40
2017-06-28 22:49:07	I	22.5	40
2017-06-28 22:49:59	I	45.0	40
2017-06-28 22:50:48	I	67.5	40
2017-12-30 00:48:20	V	0.0	200
2017-12-30 00:51:52	V	22.5	200
2017-12-30 00:55:25	V	45.0	200
2017-12-30 00:58:58	V	67.5	200
2017-12-30 01:02:32	V	0.0	200
2017-12-30 01:06:05	V	22.5	200
2017-12-30 01:09:38	V	45.0	200
2017-12-30 01:13:10	V	67.5	200

Table B.3. Observations log for SN 2018bgv.

Date and time (UTC)	Filter	HWP angle (°)	Exposure (s)
2018-05-24 00:43:09	V	0.0	500
2018-05-24 00:51:39	V	22.5	500
2018-05-24 01:00:11	V	45.0	500
2018-05-24 01:08:41	V	67.5	500
2018-06-04 21:11:26	V	0.0	500
2018-06-04 21:19:56	V	22.5	500
2018-06-04 21:28:26	V	45.0	500
2018-06-04 21:36:55	V	67.5	500
2018-06-12 22:20:44	V	0.0	600
2018-06-12 22:30:54	V	22.5	600
2018-06-12 22:41:04	V	45.0	600
2018-06-12 22:51:14	V	67.5	600
2018-06-26 21:20:33	V	0.0	400
2018-06-26 21:27:23	V	22.5	400
2018-06-26 21:34:15	V	45.0	400
2018-06-26 21:41:05	V	67.5	400
2018-06-26 21:47:56	V	0.0	400
2018-06-26 21:54:46	V	22.5	400
2018-06-26 22:01:36	V	45.0	400
2018-06-26 22:08:26	V	67.5	400
2018-07-12 21:25:25	V	0.0	550
2018-07-12 21:34:46	V	22.5	550
2018-07-12 21:44:07	V	45.0	550
2018-07-12 21:53:27	V	67.5	550
2018-07-12 22:02:48	V	0.0	550
2018-07-12 22:12:08	V	22.5	550
2018-07-12 22:21:28	V	45.0	550
2018-07-12 22:30:49	V	67.5	550

Table B.4. Observations log for SN 2018ffj.

Date and time (UTC)	Filter	HWP angle (°)	Exposure (s)
2018-08-26 04:46:16	V	0.0	600
2018-08-26 04:56:26	V	22.5	600
2018-08-26 05:06:38	V	45.0	600
2018-08-26 05:16:48	V	67.5	600
2018-09-08 04:41:24	V	0.0	500
2018-09-08 04:49:54	V	22.5	500
2018-09-08 04:58:23	V	45.0	500
2018-09-08 05:06:53	V	67.5	500
2018-09-08 05:15:25	V	0.0	500
2018-09-08 05:23:55	V	22.5	500
2018-09-08 05:32:25	V	45.0	500
2018-09-08 05:40:55	V	67.5	500
2018-09-19 02:49:14	V	0.0	500
2018-09-19 02:57:44	V	22.5	500
2018-09-19 03:06:14	V	45.0	500
2018-09-19 03:14:44	V	67.5	500
2018-09-19 03:23:16	V	0.0	500
2018-09-19 03:31:47	V	22.5	500
2018-09-19 03:40:17	V	45.0	500
2018-09-19 03:48:47	V	67.5	500

Table B.5. Observations log for SN 2019neq.

Date and time (UTC)	Filter	HWP angle (°)	Exposure (s)
2019-09-03 21:10:31	V	0.0	500
2019-09-03 21:18:59	V	22.5	500
2019-09-03 21:27:28	V	45.0	500
2019-09-03 21:35:56	V	67.5	500
2019-09-08 21:11:49	V	0.0	500
2019-09-08 21:20:17	V	22.5	500
2019-09-08 21:28:46	V	45.0	500
2019-09-08 21:37:14	V	67.5	500
2019-09-16 20:32:59	V	0.0	500
2019-09-16 20:41:27	V	22.5	500
2019-09-16 20:49:56	V	45.0	500
2019-09-16 20:58:24	V	67.5	500
2019-09-25 21:13:24	V	0.0	650
2019-09-25 21:24:22	V	22.5	650
2019-09-25 21:35:20	V	45.0	650
2019-09-25 21:46:19	V	67.5	650

Table B.6. Observations log for SN 2020tcw.

Date and time (UTC)	Filter	HWP angle (°)	Exposure (s)
2020-10-15 19:51:17	V	0.0	250
2020-10-15 19:55:36	V	22.5	250
2020-10-15 19:59:54	V	45.0	250
2020-10-15 20:04:12	V	67.5	250
2021-01-19 05:59:18	V	0.0	500
2021-01-19 06:07:46	V	22.5	500
2021-01-19 06:16:15	V	45.0	500
2021-01-19 06:24:45	V	67.5	500
2021-01-19 06:33:15	V	0.0	500
2021-01-19 06:41:43	V	22.5	500
2021-01-19 06:50:12	V	45.0	500
2021-01-19 06:58:40	V	67.5	500

Table B.7. Imaging polarimetry observations obtained with VLT/FORS2 for SN 2017gci and NOT/ALFOSC for the five SLSNe-I. The measurements of SN 2018ibb are presented in Schulze et al. (in prep).

Date	MJD (d)	Phase[a] (d)	FWHM (pixel)	S/N Ratio	Q (%)	U (%)	$P^{(b)}$ (%)	θ (°)
SN 2017egm								
V band								
2017-06-19	57923.9	−2.2	3.29	601.80	0.34 ± 0.36	0.15 ± 0.40	0.25 ± 0.38	11.9 ± 28.3
2017-06-28	57932.9	6.5	5.48	501.13	0.23 ± 0.37	0.02 ± 0.40	0.13 ± 0.39	2.5 ± 45.6
R band								
2017-06-17	57921.9	−4.2	4.16	568.31	0.15 ± 0.36	0.15 ± 0.40	0.12 ± 0.38	22.5 ± 51.4
2017-06-19	57923.9	−2.2	3.81	604.59	0.25 ± 0.36	0.34 ± 0.40	0.30 ± 0.38	26.8 ± 26.2
2017-06-28	57932.9	6.5	5.84	507.42	0.38 ± 0.37	−0.07 ± 0.40	0.26 ± 0.39	−5.2 ± 27.4
I band								
2017-06-19	57923.9	−2.2	3.10	499.98	−0.16 ± 0.37	−0.33 ± 0.40	0.25 ± 0.39	−57.9 ± 31.1
2017-06-28	57932.9	6.5	5.27	394.91	0.49 ± 0.38	0.44 ± 0.42	0.54 ± 0.40	21.0 ± 17.4
SN 2017gci								
V band								
2017-08-29	57994.4	7.0	0.00	1085.69	−0.05 ± 0.06	−0.05 ± 0.06	0.05 ± 0.06	−67.6 ± 25.5
2017-09-23	58019.3	29.9	0.00	767.70	0.06 ± 0.09	0.20 ± 0.09	0.19 ± 0.09	36.1 ± 12.5
2017-10-19	58045.3	53.8	0.00	542.84	−0.44 ± 0.13	0.34 ± 0.13	0.54 ± 0.13	71.1 ± 6.6
2017-12-17	58104.2	108.0	0.00	350.99	−0.32 ± 0.20	−0.09 ± 0.20	0.28 ± 0.20	−82.0 ± 17.4
SN 2018bgv								
V band								
2018-05-24[c]	58262.0	5.3	4.33	279.36	0.14 ± 0.25	0.03 ± 0.26	0.08 ± 0.26	6.0 ± 50.1
2018-06-04	58273.9	16.3	4.76	354.19	0.49 ± 0.21	0.62 ± 0.19	0.76 ± 0.20	25.8 ± 7.2
2018-06-12	58281.9	23.8	5.47	269.97	0.18 ± 0.26	0.37 ± 0.26	0.34 ± 0.26	32.0 ± 18.1
2018-06-26[d]	58295.9	36.7	5.99	89.45	3.69 ± 0.81	1.75 ± 0.78	4.01 ± 0.80	12.7 ± 5.7
2018-07-12[d]	58311.9	51.6	10.84	82.91	3.27 ± 0.86	0.75 ± 0.84	3.25 ± 0.85	6.5 ± 7.3
SN 2018ffj								
V band								
2018-08-26[d]	58356.2	15.1	4.13	75.94	0.43 ± 0.96	−1.70 ± 0.91	1.50 ± 0.94	−37.9 ± 14.9
2018-09-08	58369.2	25.6	3.33	280.14	−0.44 ± 0.25	−0.07 ± 0.26	0.37 ± 0.26	−85.2 ± 16.1
2018-09-19	58380.2	34.5	3.39	176.82	0.37 ± 0.40	−0.04 ± 0.40	0.25 ± 0.40	−3.5 ± 30.8
SN 2019neq								
V band								
2019-09-03	58729.9	−3.7	3.69	634.85	0.07 ± 0.11	−0.12 ± 0.11	0.11 ± 0.11	−30.2 ± 22.7
2019-09-08[c]	58734.9	0.8	9.92	237.53	−0.78 ± 0.30	0.71 ± 0.30	1.01 ± 0.30	68.9 ± 8.2
2019-09-16	58742.9	8.0	3.52	453.49	−0.32 ± 0.16	−0.10 ± 0.16	0.29 ± 0.16	−81.7 ± 14.0
2019-09-25	58751.9	16.2	5.92	434.88	−0.31 ± 0.16	0.09 ± 0.16	0.28 ± 0.16	81.5 ± 14.5
SN 2020tcw								
V band								
2020-10-15	59137.8	7.3	5.67	576.84	0.15 ± 0.17	0.01 ± 0.17	0.10 ± 0.17	1.1 ± 30.9
2021-01-19	59233.3	96.9	4.01	502.44	0.03 ± 0.18	−0.08 ± 0.18	0.05 ± 0.18	−34.0 ± 57.0

[a] Rest frame days with respect to peak MJDs shown in Table 1. [b] Bias-corrected polarisation degree. Measurements whose error is larger than the value are consistent with zero polarisation. [c] The results are unreliable due to the high lunar illumination and are therefore excluded. [d] The low S/N makes the results unreliable and are therefore excluded.

Appendix C: Figures

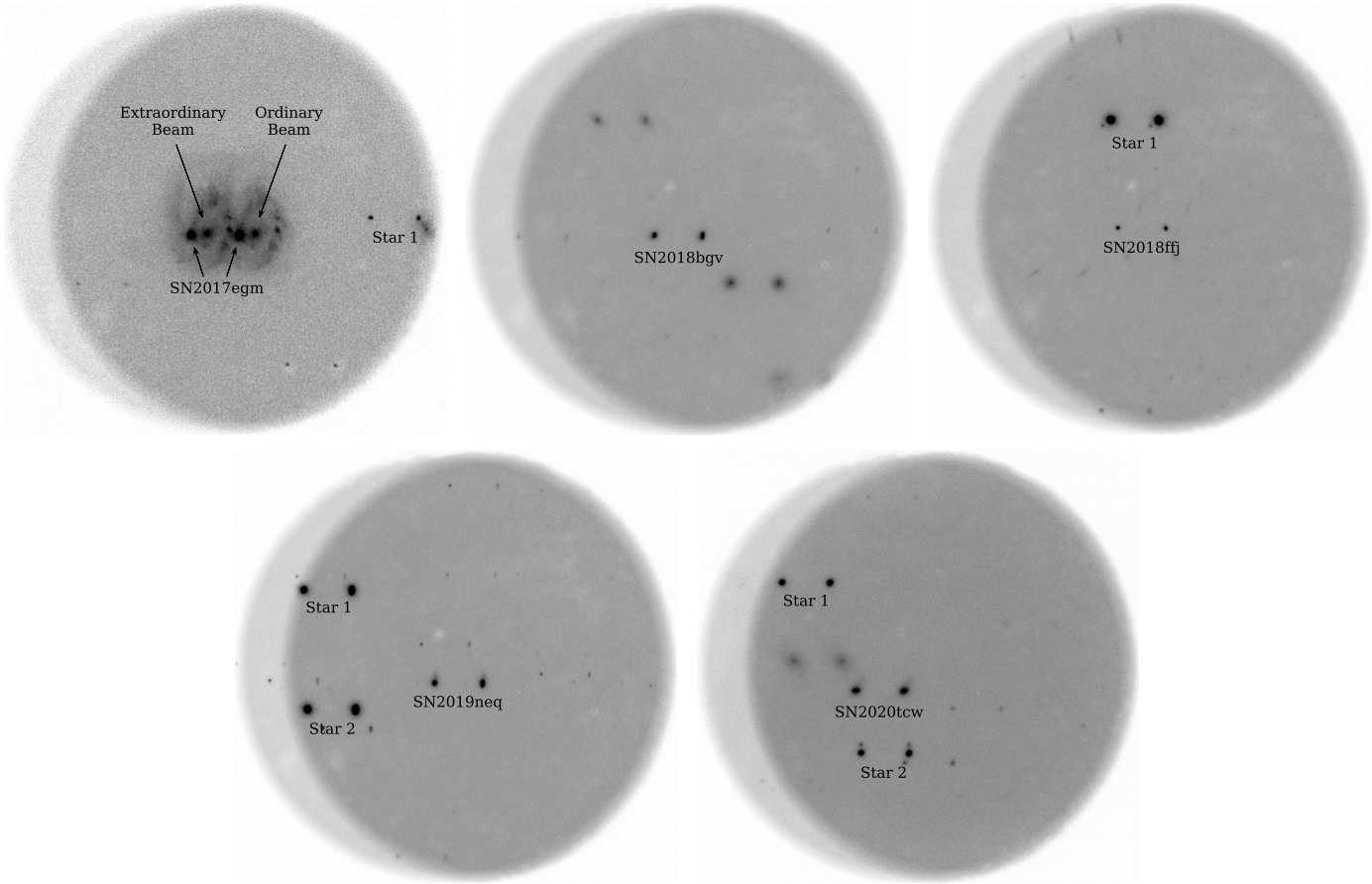

Fig. C.1. Example NOT/ALFOSC polarimetry images for SN 2017egm, SN 2018bgv, SN 2018ffj, SN 2019neq and SN 2020tcw. In the polarimetric mode, the *e* (left) and *o* beams (right) are overlaid with an offset of 15″. In addition to the SNe, bright point sources (i.e. stars) have been marked in the images. For SN 2017egm, Star 1 is located on the edge of the *e* beam image and is unreliable to estimate the ISP. No stars are present in the FOV of SN 2018bgv. Star 1 was used to estimate the ISP for SN 2018ffj. For SN 2019neq, only Star 2 is used to determine the ISP as Star 1 is found on the edge of the *o* beam image resulting in an unreliable ISP estimate. Only Star 1 is used to estimate the ISP of SN 2020tcw as Star 2 has several objects in the close vicinity and the ISP cannot be reliably identified.

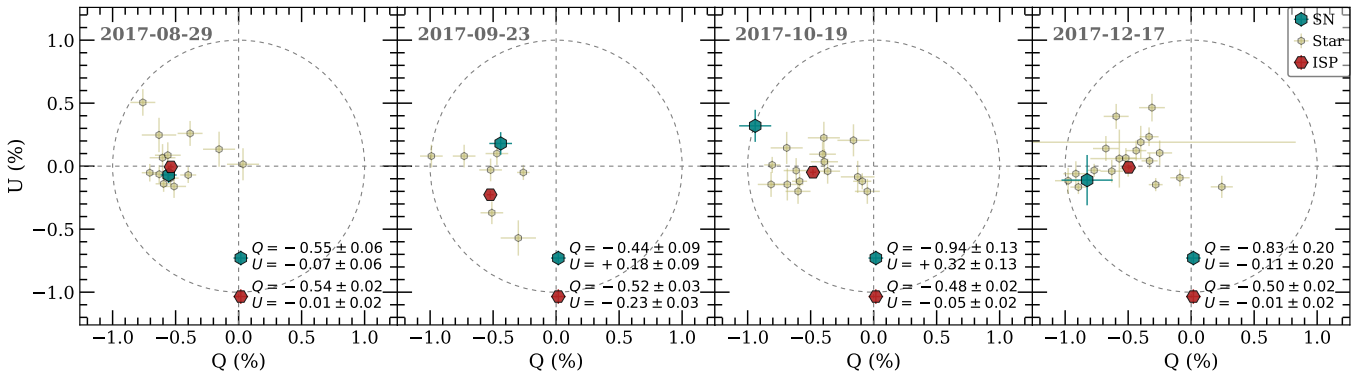

Fig. C.2. Stokes parameters of SN 2017gci and bright field stars measured at four epochs displayed on the $Q-U$ plane. The SN (teal) and the field stars passing the selection criteria (olive) as well as derived Galactic ISPs (red) are shown. The second epoch consists only one cycle of observations, making the ISP estimate less reliable. For the other three epochs the derived values of ISP are consistent.

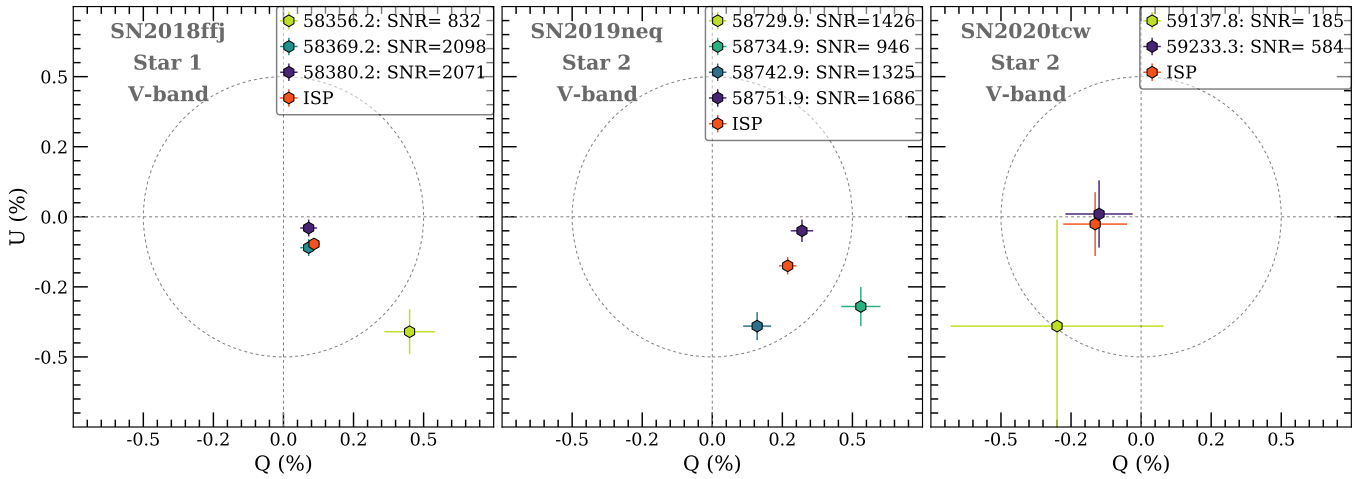

Fig. C.3. $Q-U$ planes for the stars used to measure the ISP for SN 2018ffj, SN 2019neq and SN 2020tcw. We note that the star was saturated in the first epoch of SN 2019neq and it is excluded and that the first epoch of SN 2018ffj and the second epoch of SN 2019neq were excluded due to the high lunar illumination (see Section 2.2).

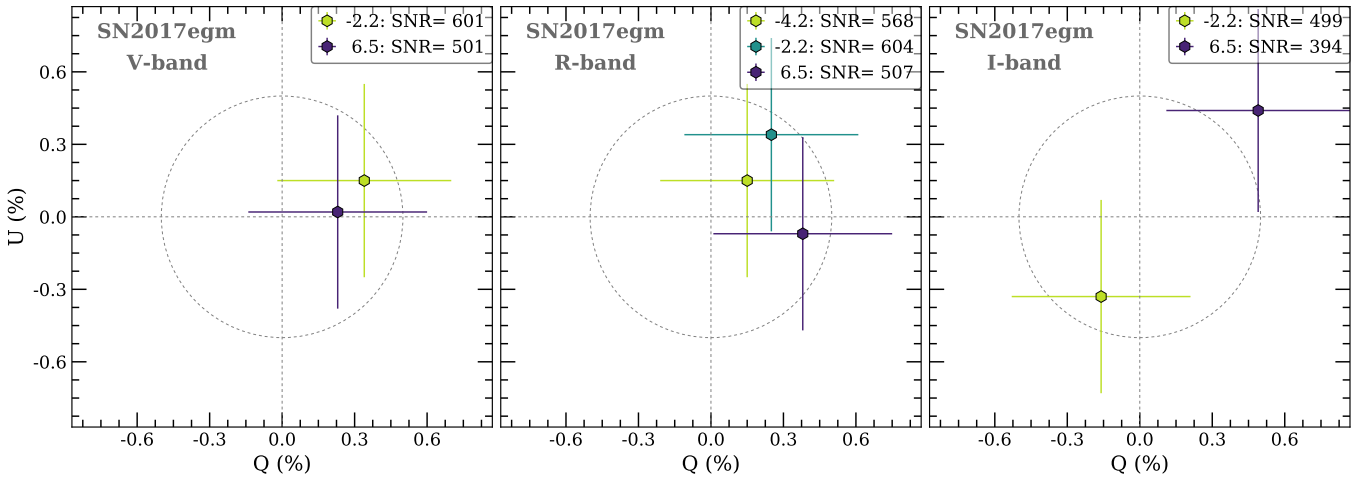

Fig. C.4. $Q-U$ planes for the ISP corrected polarimetry of SN 2017egm in *VRI* bands. We note that the last epoch of NOT polarimetry is not shown in the figure due to extremely poor observing conditions (see Section 2.2)

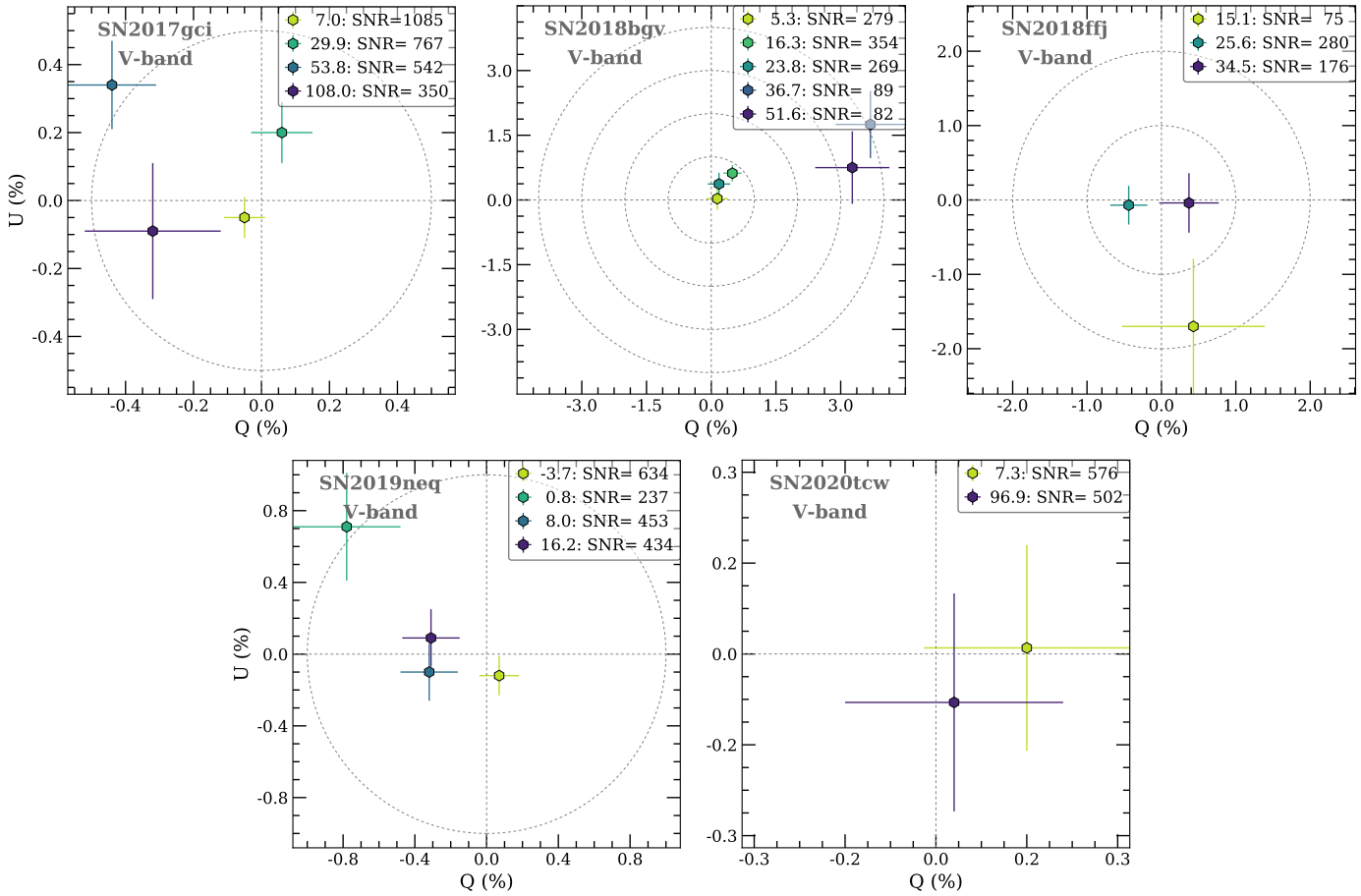

Fig. C.5. $Q - U$ planes of ISP-corrected polarimetry for SN 2017gci, SN 2018bgv, SN 2018ffj, SN 2019neq and SN 2020tcw. We note that the two last epoch of SN 2018bgv and first epoch of SN 21018ffj were excluded from the analysis due to low S/N and the second epoch of SN 2019neq due to the bright Moon (see Section 2.2)

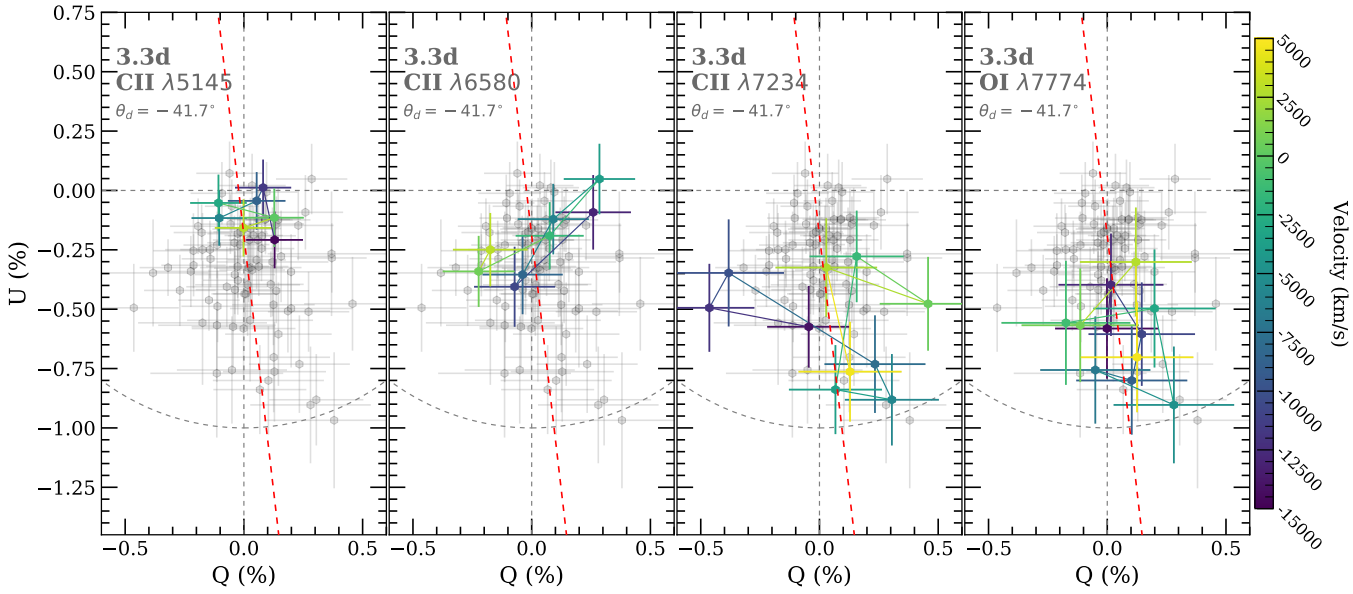

Fig. C.6. Notable line features on the $Q - U$ plane of SN 2017gci at 3.3 d. The line regions are highlighted by velocities as indicated by the colour bar, while other data points are shown in grey. The dominant axis from Figure 3 is shown in dashed red. No loop-like structures are seen, but C II λ6580 shows tentative deviation from the dominant direction.

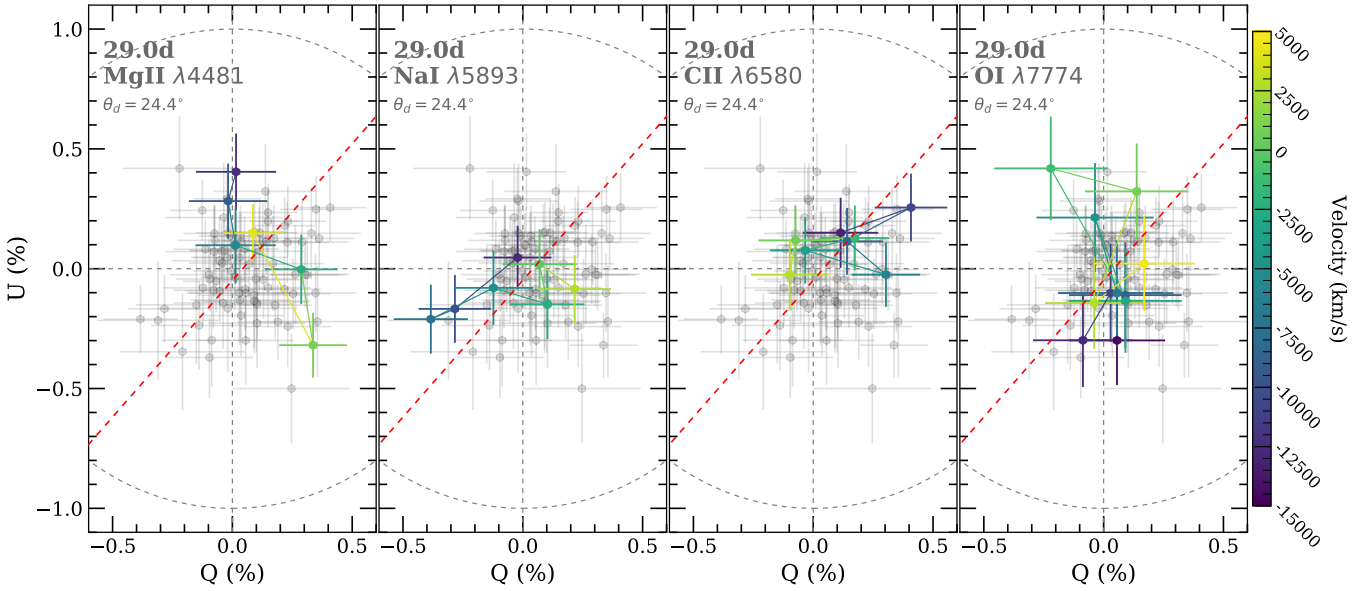

Fig. C.7. Same as Figure C.7 but for 29.0 d. No notable loops are present. Despite no clear tendency was seen in Figure 3, Mg II λ4481 is tentatively orthogonal to the shown dominant axis while Na I λ5893 and possibly C II λ6580 are along it.